X-ray fluorescence and laser-induced breakdown spectroscopy for the sorting of WC-Co hardmetal scrap based on their chromium content

Master's Thesis, 10.6.2022

Author:

Tuure Rantanen

Supervisors:

Mikko Laitinen
Teemu Karhumaa (Tikomet)

UNIVERSITY OF JYVÄSKYLÄ
DEPARTMENT OF PHYSICS

Abstract

Rantanen, Tuure
X-ray fluorescence and laser-induced breakdown spectroscopy for the sorting of tungsten carbide cobalt hardmetal scrap based on their chromium content
Master's thesis
Department of Physics, University of Jyväskylä, 2022, 76 pages.

Tungsten carbide cobalts (WC-Co) are essential hardmetals which are used as raw material in the manufacturing of drill bits and mill grinders. As the demand for WC-Co parts grows it is of paramount importance to recycle used WC-Co pieces, both from an economical and an environmental point of view. By separating WC-Co scrap based on the amount of unwanted impurities in them, the quality of the end product increases.

In this work I tested and compared X-ray fluorescence spectroscopy (XRF) and laser-induced breakdown spectroscopy (LIBS) techniques in the elemental analysis of WC-Co scrap. The impurity element of interest was chromium and the two techniques were compared for their suitability in the detection of chromium from WC-Co scrap pieces. The analysis of the measured XRF and LIBS spectra focused on the characteristic X-ray energies and the atomic emission of lines of chromium, respectively.

I used three different setups for XRF and two for LIBS to identify how they affect the results of the measurements. Both techniques turned out to be reliable in telling the difference between samples that contained 0.00 and 0.45 % Cr. However, only XRF was able to differentiate reliably between 0.00 and 0.19 % Cr samples. The most promising positions at the spectra for the detection of chromium were the presence or absence of a peak at Cr Kα (about 5.4 keV) in XRF spectra and at 425.44 nm in LIBS spectra. These positions had the least interference in and around them, and so they can be good indicators for chromium in a sample.

Keywords: X-ray fluorescence, laser-induced breakdown spectroscopy, hardmetal, tungsten carbide cobalt

Tiivistelmä

Rantanen, Tuure
Röntgenfluoresenssin ja laser-indusoidun plasmaspektroskopian käyttö volframikarbidikoboltti-jätepalojen lajittelussa niiden kromipitoisuuden perusteella
Pro gradu -tutkielma
Fysiikan laitos, Jyväskylän yliopisto, 2022, 76 sivua

Volframikarbidikoboltit (WC-Co) ovat tärkeitä kovametalleja poranterien ja jyrsinten terien raaka-aineena. WC-Co:sta valmistettujen osien kysynnän kasvaessa on sekä ekologisesti että taloudellisesti järkevää kierrättää käytetyt WC-Co-palat. Kierrätyksestä saatavan raaka-aineen laatua voidaan parantaa erottelemalla kierrätykseen saapuvat WC-Co-palat niiden sisältämien epäpuhtauksien perusteella.

Tässä tutkielmassa testasin ja vertailin röntgenfluoresenssispektroskopiaa (XRF) ja laser-indusoitua plasmaspektroskopiaa (LIBS) WC-Co-palojen alkuaineanalyysissä. Analysoin tekniikoiden sopivuutta kromin havaitsemiseen näistä WC-Co-näytepaloista. Analyysin keskiössä olivat kromin karakteristiset energiat XRF:ssä sekä emissioviivat LIBS:ssä.

Käytin XRF-mittauksissa kolmea eri mittausasetelmaa ja LIBS-mittauksissa kahta, jotta sain selville niiden vaikutukset mittauksiin. Molemmat tekniikat osoittautuivat luotettaviksi 0,00 ja 0,45 % kromia sisältävien näytteiden erottamiseen toisistaan. Tekniikoista vain XRF pystyi luotettavasti erottamaan 0,00 ja 0,19 % kromia sisältävät näytteet toisistaan. XRF-spektreissä lupaavin alue kromin tunnistamiseen oli Cr Kα (n. 5,4 keV) energian kohdalla, kun taas LIBS-spektreissä lupaavin alue oli 425,44 nm kohdalla. Näillä kohdin esiintyi vähiten muiden aineiden aiheuttamaa häiriötä ja piikit erottuivat selkeästi muusta spektristä, joten ne vaikuttavat hyviltä kohdilta kromin havaitsemiseen.

Avainsanat: Röntgenfluoresenssi, laser-indusoitu plasmaspektroskopia, kovametalli, volframikarbidikoboltti

Preface

I am grateful to Mikko Laitinen and Teemu Karhumaa for introducing me to this thesis opportunity and for guiding me through it. An interesting topic and a practical perspective to it was just the thing I needed as the basis of my thesis. In addition to my supervisors, I also want to thank people who guided and assisted me with different parts of this project: Janne Yliharju for XRF-related measurements as well as Saara Kaski, Heikki Häkkänen, Juha Toivonen, and Joni Ahokas for LIBS-related measurements.

Special thank you goes to my family for showing interest in what I do and for being such a wonderful family to have had been grown up with. I also want to thank you my girlfriend Laura for having patience with me during stressful moments and for cheering me up during the lowest of lows during this project. Shoutout to Tatu Korkiamäki for imaging the LIBS craters of my samples with SEM. And finally, big thank you to all the people I have befriended during these years I have studied in Jyväskylä, it is because of you that I managed to get to this point of thanking you in this preface.

Jyväskylä June 10, 2022

Tuure Rantanen

Contents

1 Introduction

Modern industry is on the brink of change. Environmental effects need to be taken into account in every step of product lifetime, especially when these products reach the end of their lifespan. Recycling is the key to decreasing the need for virgin resources in the industry. However, recycling processes need to be cost efficient and the resources obtained from the processes need to be of high quality.

Elemental analysis is an important part of recycling processes in many fields of industry. It is essential to know what elements the recycled object contains since impurities can affect the quality of the end product of the recycling process. Thus, determining the composition of the recycled objects and separating different quality objects can improve the end result, resulting in higher quality and higher value resources. This provides both an environmental and economic incentive to ensure that this procedure is carried out. This is especially true in the tungsten carbide cobalt (WC-Co) industry.

WC-Co is a hardmetal which consists of tungsten carbide particles adhered together by cobalt. It is an ideal material for applications that require hardness and durability, e.g. cutting and crushing tools. One of the recycling processes for WC-Co scrap is the zinc process which is a relatively straightforward process. Using liquid zinc the hardmetal bits are broken down into tungsten carbide particles and cobalt. Furthermore, since the crystal structure of the tungsten carbides does not change in this process, they can readily be reused for products that require similar crystal structures [1].

Currently about 46 % of tungsten carbide products are recycled and one of the reasons why virgin tungsten carbide is preferred over recycled tungsten carbide is higher impurity levels of the recycled product compared to the virgin product [2]. Ensuring that the products of the recycling process are as high quality as possible reduces the need for acquisition of virgin material through mining or other means [3]. As recycled tungsten carbide is an increasingly important source of raw tungsten carbide in the future, improving the quality of it is essential for companies working in this field of industry [4]. This can be achieved through elemental analysis of WC-Co scrap with e.g. X-ray fluorescence and laser-induced breakdown spectroscopy.

X-ray fluorescence (XRF) has been used in elemental analysis of many different

materials [5–7], including WC-Co [8, 9]. This technique is based on the excitation and de-excitation of atomic electrons in the sample. When the sample is exposed to incident X-radiation, the atoms of the sample have a chance of absorbing these incident photons by emitting an electron from an inner electron shell. As the outer shell electrons then move to the vacant positions at lower energy shells X-ray photons are emitted. These photons have characteristic energies that depend on which elements they originate from. Detecting these photons produces a spectrum from which the elemental composition of the sample can be determined. Figure 1a shows the principle of operation of an XRF spectrometer.

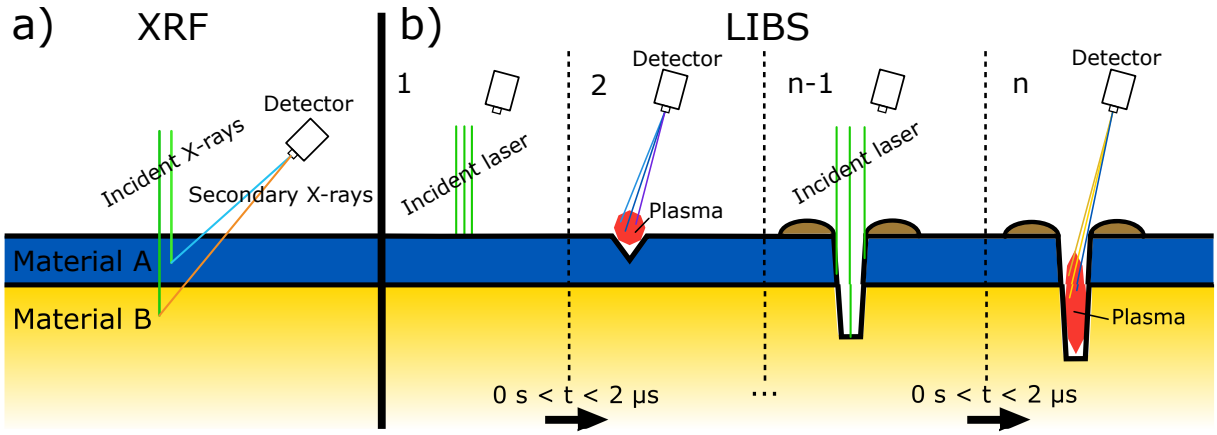

Figure 1. The principles of a) X-ray fluorescence and b) laser-induced breakdown spectroscopy in elemental analysis of a multilayered sample.

Laser-induced breakdown spectroscopy (LIBS) is an important technique in industrial elemental analysis of samples that can be damaged during the measurement process [10–12]. Tungsten carbide industry has used LIBS in many projects to determine elemental compositions of tungsten carbides [13, 14]. Incident laser pulse is used to ablate an area of the sample surface into a plasma cloud. Since the plasma consists of the same atoms as the surface from which it originated, measuring the spectrum of the plasma reveals information about the composition of the sample surface. In this technique the detected photons originate from a plasma, they are near visible light in energy, and the sample is damaged in the process. Use of multiple consecutive laser pulses allows this technique to make a hole to the sample surface, and if the surface material layer is not too thick, the composition of the underlying material can also be determined. The operation principle of a LIBS spectrometer is presented in Figure 1b.

The aim of this work is to evaluate the use of XRF and LIBS in detection of chromium (Cr) impurities in WC-Co scrap pieces. The fundamentals of the techniques are described and they are compared in terms of how well they can distinguish between various Cr

percentages. The effect of the coating on some of the scrap pieces on the measurements is also investigated. Furthermore, the properties and demands of these techniques are compared to determine which of them is more suitable for future use in the separation of WC-Co scrap pieces by their Cr content.

2 Background of X-ray fluorescence

X-rays were first discovered by Wilhelm Conrad Röntgen in 1895, for which he was awarded the first Nobel Prize in Physics in 1901 [15, 16]. X-rays are a part of electromagnetic radiation spectrum, traditionally the part which includes wavelengths between roughly 10 pm and 10 nm is considered to be X-rays [17]. The corresponding energy range is between 124 eV and 124 keV. X-rays are ionising radiation because their energy is high enough to ionise the atoms or molecules of the medium through which the radiation passes.

2.1 Characteristic X-rays

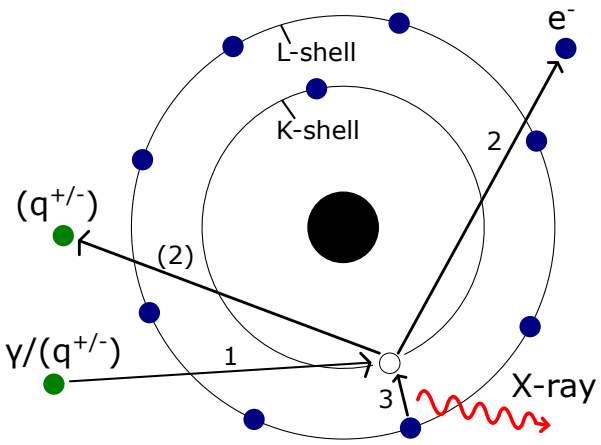

Figure 2. Formation of characteristic radiation. 1) An incoming photon (or a charged particle) interacts with an electron from the K-shell of an atom. 2) An electron (and the charged particle) is emitted from the atom. 3) The hole left behind in the K-shell is filled when an electron from an outer shell transitions into the K-shell and a characteristic X-ray photon is emitted. [18]

In Figure 2, an incident photon, or a charged particle such as an electron or an atomic nucleus, with sufficient energy interacts with an electron in one of the inner-shells of an atom. The energy of the incident photon or particle needs to be more than the binding energy of the bound electron for the electron to gain enough energy to exit the atom as a photoelectron, leaving a hole behind in the shell from which it left.

An outer shell electron transitions into this hole and as it does so, it emits a photon with the energy matching the transition energy. This photon is called a characteristic photon. The energy of this characteristic photon is equal to the energy difference between the shell to which the electron transitioned to and the shell to which it transitioned from. Since the energy of the emitted photon depends on the energy difference of the initial and final shells, an atom can emit characteristic photons only of certain distinctive energies determined by the energy differences of its electron shells. As all elements have different electron binding energies at different shells, the characteristic X-rays can be used to determine the element from which it originated from.

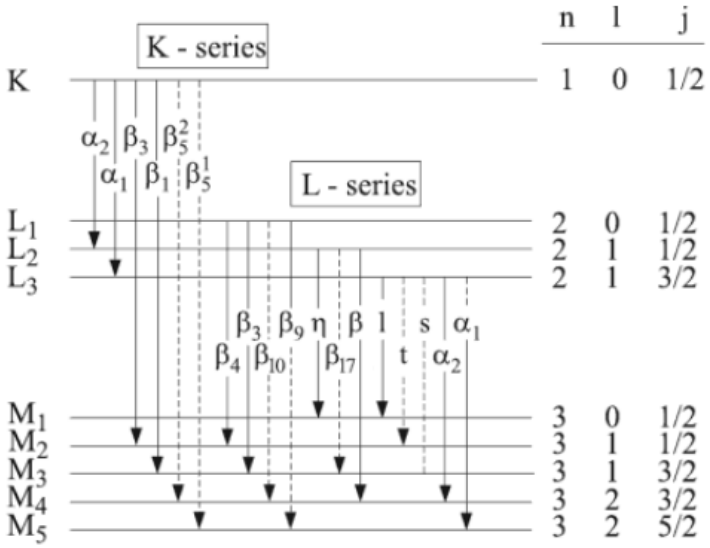

Figure 3. Grotrian diagram of the K-, L- and M series of X-ray transitions. The Greek letters show the Siegbahn notation of the transition and the IUPAC notation can be deducted from the shell names in the left side of the diagram. The solid arrows in the diagram present allowed dipole transitions and the dashed arrows present higher multipolarity transitions. [19]

The characteristic X-rays generally have two notations in use: the Siegbahn notation and the IUPAC notation. They are both based on the shells that are part of the transition. The Siegbahn convention begins with the letter of the shell to which the electron transitions to and the second letter is a Greek letter α, β, γ... denoting the shell level difference followed by an Arabic numeral subscript that depends on the sub-shell from which the electron transitions. [17]

The IUPAC naming convention includes the letters of the inner-shell and the outer-shell separated by a hyphen (-). After each letter, the sub-shell of the shell in question is

described by an Arabic numeral subscript. [20] For example, the subscript number for the lowest-energy sub-shell is 1, for the second-lowest sub-shell 2 and so forth.

The energy levels of the electron shell and the transitions are shown in Figure 3. For example, an X-ray emitted when an electron transitions from M_2-shell to K-shell is called $K\beta_3$ (Siegbahn) and K-M_2 (IUPAC) and an X-ray from M_5-shell to L_3-shell transition is called $L\alpha_1$ (Siegbahn) and L_3-M_5 (IUPAC).

2.2 Bremsstrahlung

In addition to characteristic radiation, there is another type of X-radiation called bremsstrahlung. Bremsstrahlung occurs when a charged particle, typically an electron, is decelerated by the deflection effect of an electric field, such as that of an atomic nucleus, as can be seen in Figure 4. The deceleration of the charged particle reduces its energy and it emits a quantum of electromagnetic radiation. The amount of energy the electron loses during the deceleration depends on the strength of the electric field that causes the deceleration. The spectrum of bremsstrahlung emitted from, e.g. X-ray tubes is always continuous because the energy emitted by the electron can vary between zero and the total kinetic energy of the electron. The maximum energy of bremsstrahlung is limited to the maximum kinetic energy of the electron.

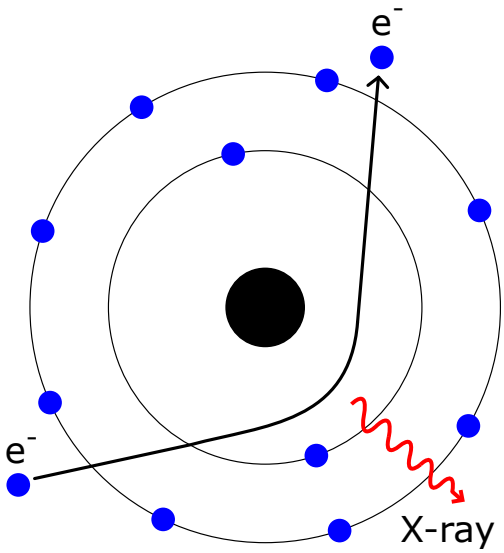

Figure 4. Formation of bremsstrahlung. An incoming electron is deflected by the electric field of an atomic nucleus. The deflection reduces the energy of the electron and it emits this excess energy as an X-ray photon. [18]

2.3 Interactions of X-rays and matter

When an X-ray photon encounters matter as it propagates through space it has a chance to interact with the atoms of the matter it comes across. The interaction can cause the atoms of the matter to ionise or might have no effect on it at all. The two interaction modes of X-rays with matter are scattering and fluorescence, and the part of X-ray beam that does not interact is transmitted through the matter [21]. Scattering can alter the energy and direction of propagation of the X-rays, and fluorescence occurs from the absorption of incident X-rays and emission of characteristic X-rays via the photoelectric effect. The intensity of the transmitted X-ray beam decreases as it propagates in the matter.

2.3.1 Rayleigh and Compton scattering

In a non-ionising interaction between an X-ray photon and an electron of an atom, two outcomes are possible. The photon can collide with the electron and retain all of its energy during the collision. This is referred to as coherent scattering or Rayleigh scattering. Since the electron gains no energy in the collision, Rayleigh scattering does not lead to the excitation or ionisation of the atom. The only difference in the properties of the photon before and after the collision can be the change in the direction of propagation. The deflection angle has a dependency on the photon energy, higher photon energies lead on average to smaller deflection angles. [21, 22]

When the interaction between an X-ray photon and a valence shell electron of the target material causes the photon to lose some of its energy to the electron in the process, it is called incoherent scattering or Compton scattering. This small gain of energy for the electron causes it to recoil, and if it is bound to an atom and the energy gained is larger than the binding energy of the electron, it causes it to become a free (recoil) electron. The photon that has been scattered in this manner has a lower energy compared to the incident photon and can propagate in a different direction. The angle of deflection of the photon determines how much of its energy is transmitted to the recoil electron. Because the photon can scatter to all possible angles, the energies of the recoil electron and the scattered photon can vary a lot. As was the case with the Rayleigh scattering, the angle of deflection is decreased on average with higher photon energies. [21, 22]

2.3.2 Photoelectric effect

An interaction between an X-ray photon and a bound electron that results in the ionisation of the atom is called photoelectric absorption. This interaction is possible if the energy of the photon is higher than the binding energy of the electron. The energy of the resulting free (photo)electron is the difference between the energy of the incident photon and the binding energy of the electron. Photoelectric absorption leaves the atom in an ionised state, and if the photoelectron originated from a non-valence shell of the atom, in an excited state. The ionised atom gains an electron by capturing a free electron from the medium surrounding it. The atom can be de-excited by the transition of an outer-shell electron in the vacancy left by the photoelectron, which results in the emission of a characteristic X-ray or an Auger electron. [21, 22]

2.3.3 Transmission

The Rayleigh and Compton scattering, as well as the photoelectric effect, cause the intensity of the incident X-ray beam to decrease as it advances into matter. The attenuation of an X-ray beam can be determined using the equation

$$I = I_0 \, e^{-\mu_m \rho x}, \tag{1}$$

where I and I_0 are the intensities of the resulting and incident beam, respectively, μ_m is the mass attenuation coefficient of the material through which the beam passes, ρ is the density of the material, and x is the distance that the incident beam has travelled in the material. [23]

2.4 X-ray fluorescence

X-ray fluorescence (XRF) is a phenomenon that is composed of the photoelectric effect of an electron in the inner shell of an atom and the emission of characteristic radiation which is the result of the de-excitation of the excited state of the atom. The characteristic radiation emitted by the atoms of the sample shows the elemental composition of the sample. The presence of an arbitrary X-ray photon of certain energy shows that the sample may contain an element that has a corresponding transition energy from one electron shell to another. The intensity of that X-ray energy shows how much of that element may be present in the sample compared to other possible elements in the sample. [24] A simplified

typical X-ray fluorescence spectrum is presented in Figure 5. The spectrum can be divided into a characteristic part and a bremsstrahlung part, of which the characteristic part is the basis for XRF analysis.

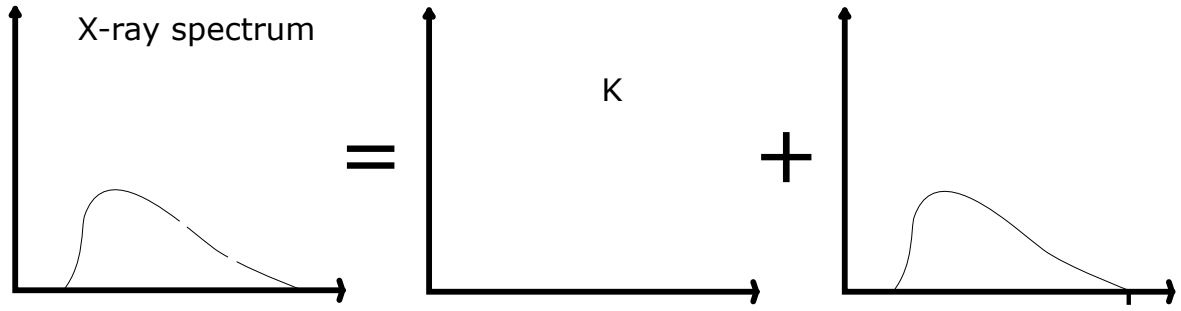

Figure 5. A typical X-ray spectrum. The spectrum has two parts: Discrete and continuous. The discrete spectrum consists of peaks that result from characteristic radiation unique to each element. The continuous spectrum consists of the bremsstrahlung.

Elements lighter than magnesium are not easily detected by their XRF because the characteristic X-rays are absorbed by the surrounding air (typically about 80 % N and 20 % O). [25, 26] The absorbing effect of air can be reduced by performing XRF in a vacuum chamber or, for example, in a helium atmosphere.

Among the advantages of XRF is the ability to measure total element concentrations. XRF does not separate between different chemical compositions in which the detected elements are present [25]. For example, if a sample contains two different compounds of titanium, such as titanium oxide and titanium nitride, XRF can not be used to determine the concentrations of those compounds. Instead XRF can tell the concentrations of the elements that the sample contains, in this case that of titanium since oxygen and nitrogen are not easily detected with XRF (in vacuum or helium atmosphere they can be detected as well). Therefore, XRF is not applicable to element analysis that aims to identify the chemical compounds as well as the elements in the sample.

XRF offers a relatively good limit of detection (LOD) of elemental composition, at best amounts around 1 to 10 ppm are detectable. This varies greatly with the sample matrix, different elements, measurement time, and the X-ray source used. [25]

XRF does not necessarily need specific sample preparations, although if the sample is homogeneous, the elemental percentages are easier to determine. Therefore, sometimes it is useful to grind or otherwise homogenise the sample for more reliable results but that can be time-consuming. Furthermore, the analysis times for XRF measurements are typically

relatively short, ranging from seconds to minutes. [25]

The use of XRF equipment in an industrial environment is common and popular in fast elemental analysis because of the simple use of the device. The process is also non-destructive and the devices can easily be made portable which widens the selection of possible applications. [25]

The limitations that hinder the use of XRF are mainly related to the selectivity, detection limits, and accuracy of the measurements. Due to the closeness of the K-lines of light elements and the L-lines of heavy elements, they can sometimes cause overlapping effects in the sample spectrum. That makes the element composition determination difficult in some cases. The earlier mentioned fact that XRF does not separate between atoms of same element in different chemical compositions means that it can not be used to get information about the chemical state of the elements of the sample. XRF cannot easily detect elements that have sub-ppm levels of occurrence in the sample, so often it is not suitable for analysis on very faint traces of elements. The fact that X-radiation is absorbed as it travels through matter means that the maximum detection depth of XRF is typically only in the range of a few mm, making it unsuitable for measuring very thick samples that consist of layers with varying compositions. As mentioned above, the accuracy of XRF is reduced for heterogeneous samples due to differing amounts of absorption in different materials. This can be avoided by homogenising the sample and using standard material samples to properly calibrate the equipment. [25]

2.5 X-ray tubes

There are many ways to produce X-rays, e.g. X-ray tubes, radioisotopes, and synchrotron radiation. The most common method used is the X-ray tube because of its relative inexpensiveness and simple yet reliable function. Figure 6 presents the two principal options for the structure of an X-ray tube. The tube itself is a housing for a cathode filament (usually made out of tungsten) and an anode (usually molybdenum, rhodium, palladium, or tungsten). On one side of the tube there is a window made of a thin film of material (typically beryllium with a thickness around 120 µm). The cathode filament is heated by running a current through it, which causes it to emit electrons in a process known as thermionic emission. Between the cathode and the anode there is a high voltage difference which causes the electrons to accelerate and move towards the anode. Inside the tube there is a vacuum to prevent air from hindering the movement of electrons from the cathode to the anode and to prevent the oxidation of the anode. When the electrons

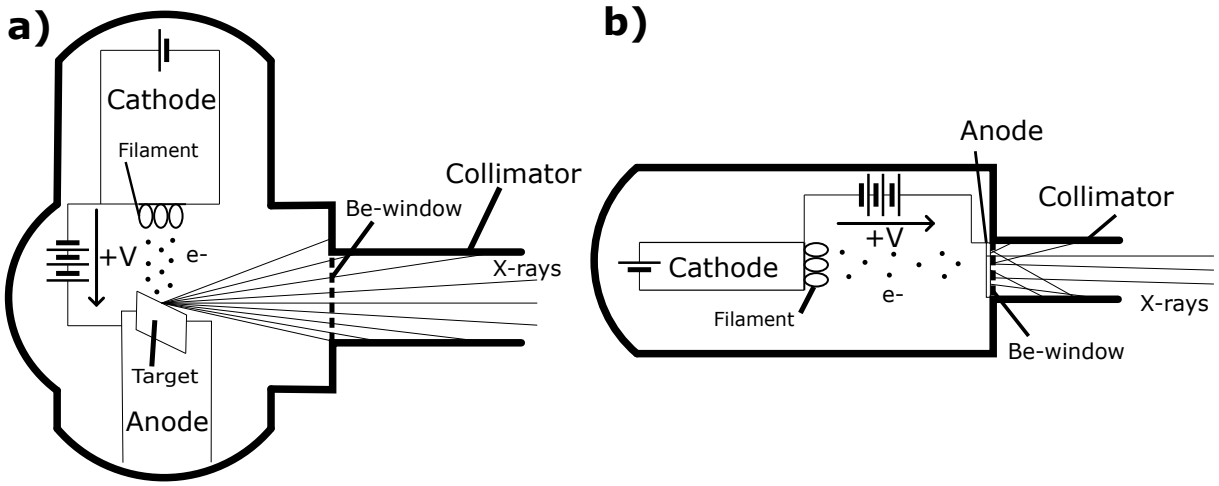

Figure 6. Simplified cross-sections of a) side-window X-ray tube and b) end-window X-ray tube.

collide with the anode, they slow down. The atoms of the target material have a possibility to be excited by the colliding electrons. Excitation results in the emission of characteristic radiation when the atoms return to their ground states. Alternatively the electrons can slow down in the medium of the target by deceleration and produce bremsstrahlung. [21, 27]

However, only a small fraction of the electrons end up emitting X-rays when colliding with the target. Most of them emit energy in the range of infrared radiation, and thus X-ray tubes accumulate a lot of heat if not cooled properly. This heating of tube structure can result in damage to the tube. Heating can be reduced by cooling the anode or using a rotating anode. Circulating water flow transfers the heat from the anode and the rotation changes the position of electron impacts which distributes the heat to a larger area of the target. [21]

The produced X-rays can exit the tube only through the thin window on the side or at the bottom of the tube. The window is typically made of beryllium because its low density and low atomic number make it a low absorption material for X-rays and it is strong enough to withstand the pressure differences between the inside and the outside of the tube. [27]

The spectrum of an X-ray tube can be divided into two parts: bremsstrahlung and characteristic radiation. The bremsstrahlung spectrum depends on the acceleration voltage used to accelerate the electrons in the tube and the current used to heat the filament cathode. The maximum energy of the bremsstrahlung is equal to the maximum kinetic

energy an electron can gain as it accelerates in the tube before colliding with the target, i.e the maximum energy of the bremsstrahlung depends on the acceleration voltage of the tube. The maximum intensity of the bremsstrahlung is determined by the amount of electrons emitted from the filament.

The positions of characteristic peaks in the spectrum of an X-ray tube depend on the elemental composition of the target. The characteristic spectrum is also affected by the filament current and the target material of the tube. The filament current can only affect the height of the peaks in the spectrum but the material of the target changes the position of the peaks.

2.6 X-ray detectors

There are several different types of X-ray detectors depending on the application in which they are used. The required detector properties vary: Health and safety devices require information about the dose and flux of X-radiation, medical imaging requires information about the spatial intensities of X-ray absorption, and material analysis requires information about the energy distribution of X-radiation.

For the purpose of X-ray fluorescence analysis, three types of detectors are widely used, those being gas-filled detectors, scintillation detectors and solid-state detectors [21]. The basic principle of each type is to transform the energy of X-ray photons into an electrical signals from which the incident energy and the flux of the photons can be determined. In the scope of this work, only two types of solid-state detectors are discussed, namely the silicon drift detector and the cadmium telluride detector.

The function of solid-state semiconductor detectors is based on the creation of electron-hole pairs. The potential difference applied over the semiconductor material in which the holes and the electrons are created forces them to drift towards the electrodes on the sides of the material. This creates a current in the detector which can be measured. Current is usually integrated in a charge-sensitive amplifier, and the amplifier outputs a voltage that is proportional to the charge created. [28]

2.6.1 Conventional detectors

Lithium drifted silicon (Si(Li)) detectors are a widely used type of X-ray detectors. Their function is based on the silicon crystal which has been diffused by lithium atoms to create different regions in the it. On the opposite sides of the crystal thin metal electrodes create an electric potential across it for the purpose of collecting the charges from it. As X-rays penetrate into the crystal, they interact with it by creating electron-hole pairs as they lose energy within the crystal. The pairs separate in the electric field and are collected at the electrodes. The charges are measured and the energy of the incident X-ray photons can be determined from the charges. In order to keep the lithium from diffusing across the whole crystal, the detector has to be cooled with liquid nitrogen, which requires an external tank of liquid nitrogen for these kind of detectors. [29] An example of the structure of a typical Si(Li) detector element can be seen in Figure 7a.

Cadmium telluride (CdTe) is a semiconductor material that can be used in X-ray detectors. The high atomic numbers of cadmium and tellurium, 48 and 50, respectively, give CdTe a high stopping power. Because of that, it is able to absorb X-rays well in the range of 40 to 150 keV. CdTe detectors have also higher sensitivity than silicon-based detectors at energies above 20 keV which is why they are better suited to the detection of K lines for elements heavier than ruthenium (Ru) [30, 31]. CdTe detectors are often constructed as a Schottky diode to reduce the leakage current in them [32]. Figure 7b shows the basic structure of a typical Schottky diode in a CdTe detector.

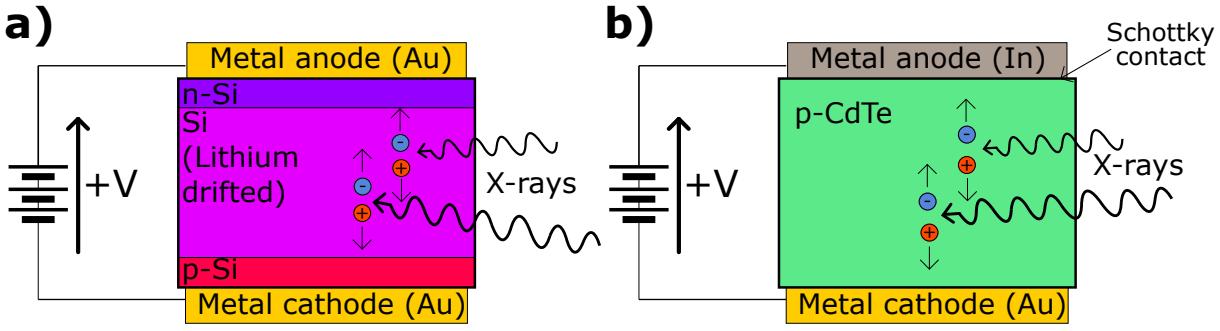

Figure 7. The detector structure of a) lithium drifted silicon (Si(Li)) detector and b) cadmium telluride (CdTe) detector. Both detectors consist of doped semiconductor crystals between two metal electrodes with a high voltage difference. In the CdTe detector, the contact between the crystal and the anode is a Schottky contact but in Si(Li) detector the contact can also be ohmic. Figures are based on similar figures in [29] and [33], respectively.

2.6.2 Silicon drift detectors

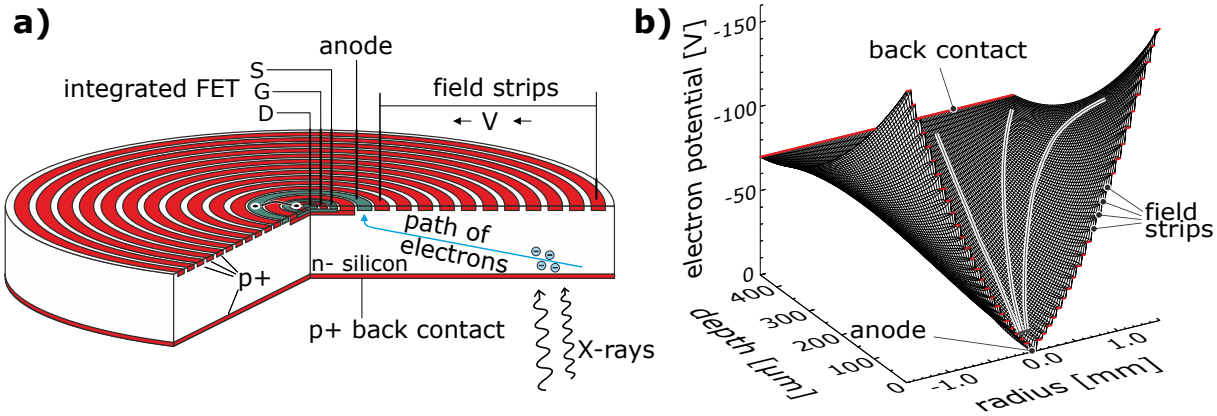

Figure 8. Figures describing a) the structure and b) the electric potential of an SDD. [34]

Silicon drift detectors (SDDs) are a type of radiation detectors made from a monocrystalline silicon chip. They measure the energies of the photons in the radiation by converting them into electrical signals. The photons that arrive at the detector transfer their energy to the electrons in the valence band of the atoms and the electrons move into the conduction band of the detector. SDDs can be divided into two subcategories based on their geometrical composition: concentric ring SDDs and teardrop SDDs. [35] The ideal design of the SDD is highly dependent on the application for which it is used, and many properties must be balanced to find the best solution. These include avoiding excess capacitance in the connections between the detector element and the electronics, shielding the connections, and cooling the detector element and the electronics. [36]

The structure of a concentric ring SDD can be seen in Figure 8a. The direction of radiation entering the detector is through the back contact. The detector is built on highly resistive silicon. Silicon is depleted from the charge carriers by applying a bias voltage at the top and bottom edges of the detector. On both sides of the silicon in Figure 8a, there are electrodes. The electrode on the side where the radiation enters the detector has a negative voltage that repels the electrons in the conduction bands of the atoms and attracts the holes in the valence band. The electrodes on the opposite side of the detector have a negative voltage approaching zero in the direction towards the anode in the centre of the rings. A visualization of the potential field that guides the electrons to the anode is presented in Figure 8b. From the anode there is a connection to a field-effect transistor (FET), which can be either discrete or integrated into the chip. If the FET is integrated it

is exposed to radiation which has enough energy to penetrate the detector, whereas if it is discrete it can be positioned to the side of the detector under its collimator. Positioned under the collimator, the discrete FET is sheltered from the bulk of the radiation and thus has less chance to be damaged by the radiation than an integrated and exposed FET. [37]

The teardrop SDD functions similar to that of the concentric-ring SDD, but its electrodes are shaped in the form of a teardrop. The electrons are led away from the centre point of the detector in an area near the outer edge of the detector, which is often shielded from the radiation by the collimator of the detector. Using this configuration, an integrated FET is protected from much of the radiation that penetrates the detector material. [37] Integrated FETs do not require external connections between them and the detector element, which decreases the capacitance of the connection between them [36].

2.6.3 Detector artefacts

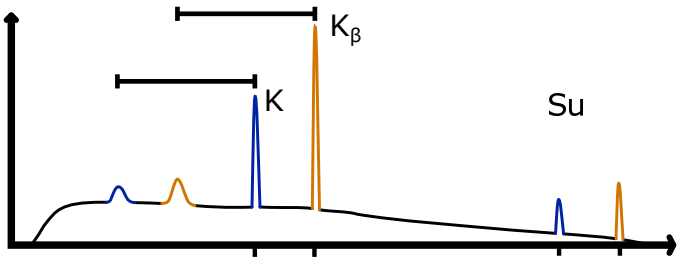

Figure 9. XRF spectrum including detector artifacts: escape peaks and sum peaks. The positions of the artifacts at the energy axis depend on the positions of the "real" peaks and the detector material. The 1.74 keV energy differences equal the characteristic energy of silicon.

Spectra which show the elemental composition of an XRF sample can have additional peaks in addition to the peaks for the elements of the sample. These kind of false peaks, often called spectrum artefacts, are very important to take into account in the analysis, otherwise they can decrease the quality of the analysis result. The spectrum artefacts that arise from the detector systems are sum peaks and escape peaks. [21] Examples of these artefacts can be seen in Figure 9.

When two ionisation events of the same energy happen at a very short time between them in the detector, there is a possibility that the detector will register these two events as only one single event. If this happens, the detector passes on the information of these

events as one event which has the combined energy of the initial events. The spectrum includes this information as a peak that can be incorrectly interpreted as the presence of an element that has a characteristic peak with that energy. [21]

Sometimes, the incoming X-rays ionise the inner-shell electrons of the atoms of the detector material. This results in the emission of characteristic radiation from the detector material. Most of this radiation is absorbed in the detector material shortly after its emission and it creates surplus charge in the charge collection of the original incident X-ray photon. Some of it does escape the detector material and does not contribute to the charge collection. In other words, those escaped X-rays mean that the energy absorbed to the detector is slightly less than if all the X-rays were absorbed in the detector. This phenomenon presents itself in the measured spectrum of the sample as an extra peak on the lower energy side of another, higher peak. The energy difference of these peaks is equivalent to the characteristic radiation energy of the detector material. If the detector material consists of multiple elements, such as CdTe, there are multiple escape peaks with energy differences from the main peak corresponding to the characteristic radiation energies of the elements in question. [21]

3 Background of laser induced breakdown spectroscopy

3.1 Laser

Light amplification by stimulated emission of radiation, or laser for short, is a technique that produces light in a limited band of wavelengths and amplifies that light.

Atoms, electrons, and molecules can absorb and emit energy via photons. When a photon is absorbed, its energy is transmitted to the particle in question and that particle becomes excited. An atom is excited if it has one or more electrons in higher energy states than the ground state. Absorption can only happen if the particle is at a lower energy level and the incident photon has energy that equals the energy difference of the two energy states involved in the process. The de-excitation of the particle can happen in two different types of emission: spontaneous or stimulated. [38] Absorption as well as both spontaneous and stimulated emission are illustrated in Figure 10.

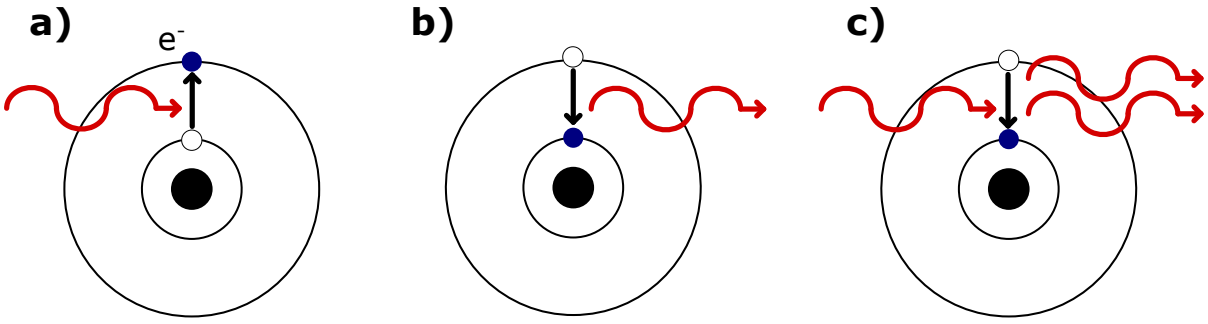

Figure 10. Excitation and de-excitation means of an atom: a) Absorption, b) spontaneous emission, and c) stimulated emission.

Spontaneous emission happens on its own, without any intervention from outside the system, and it results in an emission of a photon which has an energy equal to the difference of energy of the excited state and the state to which the particle de-excites. This emitted photon is called a resonance photon and the energy of that photon is called a resonance energy. Spontaneous emission is the main type of emission that occurs in (natural) sources of light such as the Sun and a traditional light bulb. For stimulated emission to happen, there needs to be a stimulating photon that interacts with the excited

particle. The energy of the stimulating photon must be equal to the resonance energy of the excited particle for the stimulated emission to occur. The stimulating photon disturbs the excited particle in a way which de-excites the particle into a lower energy state and emits a photon in the process. This emitted photon has the same energy, phase, and polarisation as the stimulating photon. Stimulated emission is at the heart of all laser processes and it is the key to photon multiplication. [38]

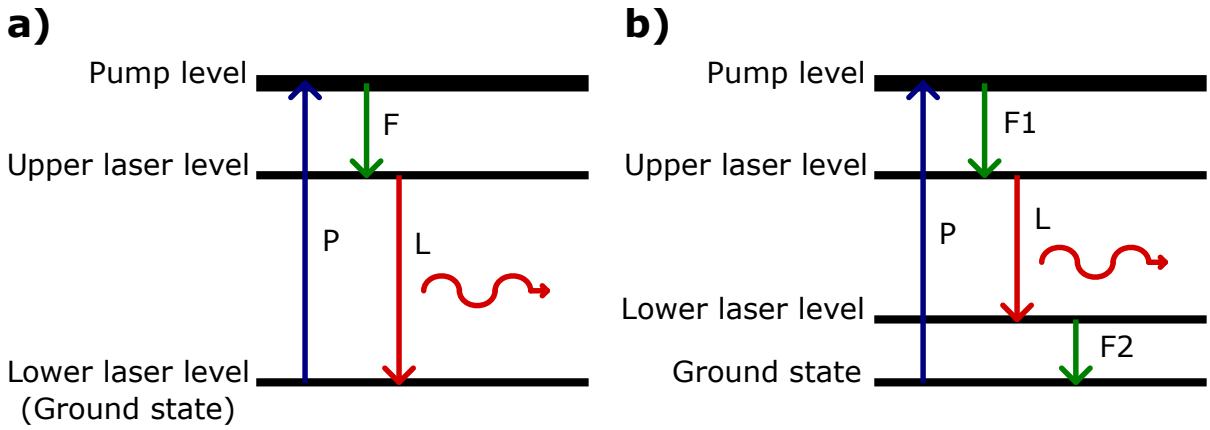

Figure 11. Energy level diagrams of a) three-level laser system and b) four-level laser system. P = Pump transition, F(1/2) = Fast and non-radiative transition, and L = Laser transition.

However, stimulated emission alone is not enough to produce laser light. Without high rates of stimulated emission and absorption when compared to spontaneous emission rate, laser action conditions are not met. The populations, number of atoms or molecules in an energy level, of lower and higher energy levels have a large impact on the rates of stimulated emission and absorption, respectively. To ensure that the rates are high enough a (pump) transition into a pump band is typically used in addition to just the two energy levels needed for stimulated emission. The atom or molecule of the laser medium is excited from the ground state into the pump level that has a relatively short lifetime. From there it transitions into the upper laser level which is a metastable level with relatively a lot longer lifetime than the pump level. This transition does not produce electromagnetic radiation and because of the metastability of the level, high number of atoms or molecules can end up at this level. If more than half of the particles of the laser medium are excited through the pump level into the upper laser level a population inversion is achieved. Now enough particles can de-excite to the lower laser level and laser action can occur. Practical laser processes can be three- or four-level systems depending on the amount of energy levels involved in the process. [38] Energy level diagrams for both of these systems are

shown in Figure 11.

3.2 Ablation of matter

A high-power laser pulse can be used to form plasma from a target material. The target can be gaseous, liquid, or solid, as long as the intensity of the laser in the focal point is enough to create intense heat, up to the plasma conditions, to the sample volume near the focal point. In the case of liquids and solids a sufficiently powerful laser pulse can evaporate a small amount of the target material. During the abaltion process this evaporated material then forms into a plasma cloud. If the duration of the laser pulse is longer than the formation time of the plasma cloud, the cloud will absorb the remaining pulse energy after its formation. [39]

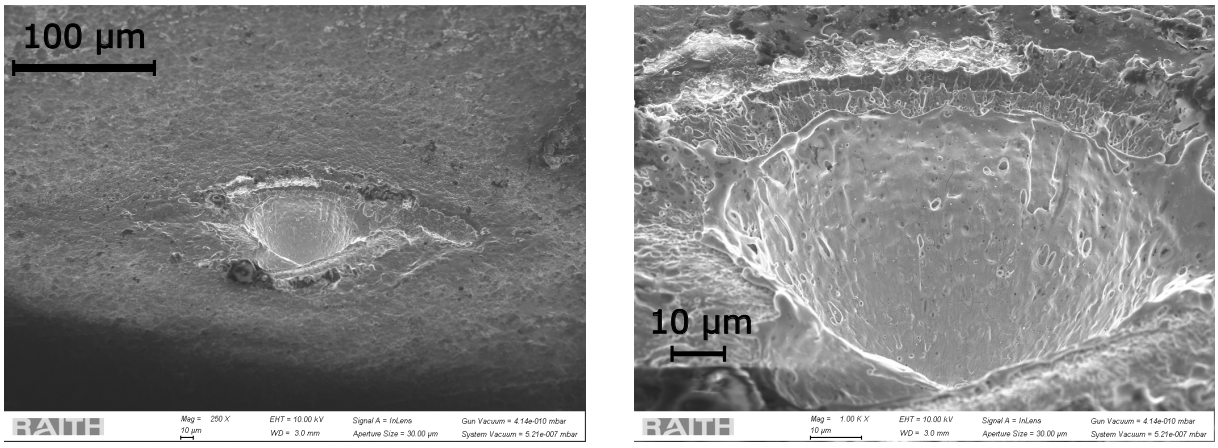

(a) **(b)**

Figure 12. a) Scanning electron microscope image of a crater formed by multiple consecutive laser pulses, b) Close-up image of the edges of the crater, both images from sample 13. Images courtesy of Tatu Korkiamäki.

The ablation of material from the surface of a solid sample leaves behind a crater on the sample surface. Through the use of multiple consecutive pulses at the same spot, the crater can be deepened further, providing optical access to the inner structure of the sample. Such a crater is shown in scanning electron microscope images in Figure 12. These kinds of craters enable depth profiling and, for example, determining the thickness of possible coatings on the samples. If the crater is too narrow, the walls of the crater can disrupt the laser pulse from reaching the bottom unobstructed which decreases the power of the laser that reaches the bottom. The material ablated by the laser may be carried away by a flow of gas, or alternatively it can condense and precipitate back to the sample

surface. This usually occurs at the edges of the crater, creating a kind of collar or barrier for the edges of the crater. Important parameters for ablation and formation of the crater are the physical and mechanical properties of the sample, such as reflectivity, density, and thermal conductivity. [39–41]

3.3 Laser-induced breakdown spectroscopy

Laser-induced breakdown spectroscopy (LIBS) is a process in which a laser pulse is used to ablate material from the sample surface. The ablated material forms plasma, and part of the electromagnetic spectrum of the plasma is then detected and analysed. A laser pulse from a laser source is first focused through a lens systemto focus it on the sample surface. When the pulse then interacts with the sample, it vaporises a part of the sample surface into a plasma cloud. A part of the spectrum of the plasma light is then directed into a spectrometer through a fiber optic system. The spectrometer separates the different wavelengths of light and displays the resulting spectrum. [42] Figure 13 presents the spectra of two elemental metals, cobalt and chromium, as an example. It shows that the LIBS spectra for different elements are very dissimilar with each other and that there are clearly detectable peaks. It also indicates that it is possible to identify individual elements from an alloy of cobalt and chromium, for example.

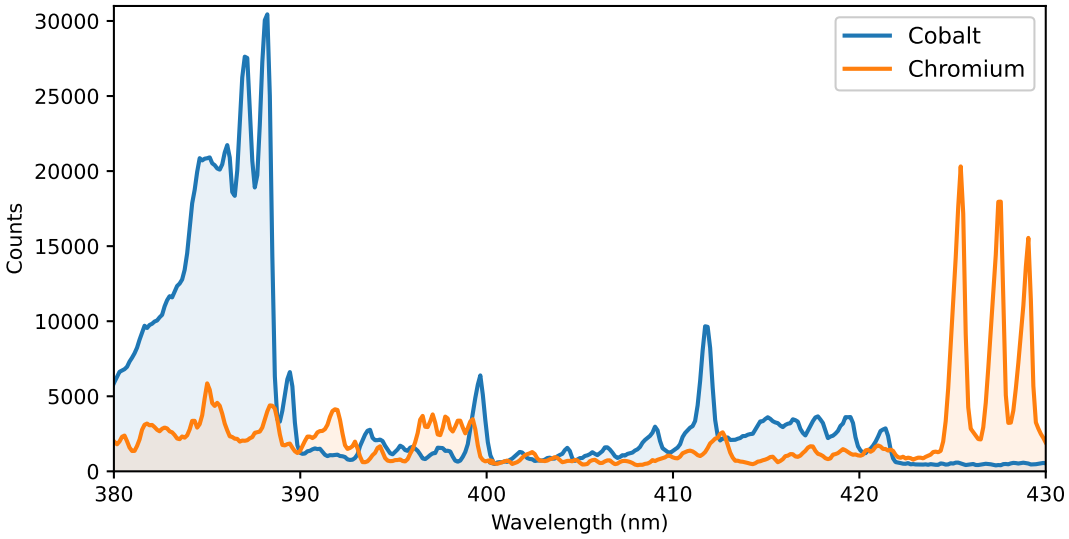

Figure 13. LIBS spectra of elemental metals cobalt and chromium. The spectra were measured with the same measurement setup and identical parameters.

The spectrum contains information about the elemental composition of the plasma.

The clarity of this information, however, depends on the length of time between the laser pulse interaction with the sample and the actual measurement of the plasma spectrum. Typically right after the plasma has formed, it emits continuous and ionic spectra because of its denseness and temperature. As it cools and expands, the intensity of the continuous spectrum decreases and the intensities of ionic and atomic spectra increase relatively in strength. This is the result of free electrons and ions recombining with each other. The clarity of the spectrum is a very important property of the plasma because unclear spectrum can be the result of too short delay between the pulse and the measurement. However, too long time is not ideal either because then the plasma has cooled and expanded so that it has disappeared or diminished so that it does not emit light anymore. [42] An example of the effect of measurement delay can be seen in Figure 14a where spectra of an elemental chromium piece measured after different delays are plotted.

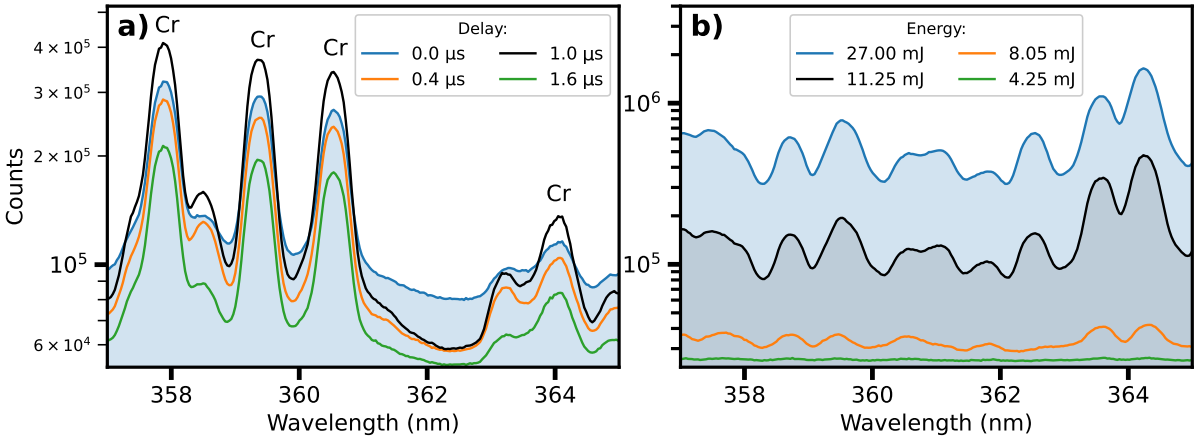

Figure 14. LIBS spectra for a) different delays between the incident laser pulse and the measurement of the spectrum of the plasma and b) different energies of the incident laser pulse. The former was performed to a piece of elemental chrome while the latter was performed to an arbitrary WC-Co sample. These spectra were measured with the setup in Tampere.

The energy of the laser pulse is also important in ensuring that formed plasma is large enough to emit significant amount of photons to the detector. As an example of the effect of laser pulse energy to the spectra, Figure 14b presents multiple spectra from the same sample with different laser energies. The shape of the spectra does not change significantly with the laser energy, however, larger number of counts does decrease the effect of noise to the smoothness of the spectra.

The elemental composition that LIBS provides is qualitative. However, with proper calibration, it can also provide quantitative information about the similar type of samples

with which the calibration was performed. [42]

3.4 Laser sources

Laser sources can be classified by many different parameters, e.g. by the type of the active medium (solid-state, semiconductor, gas) or by the produced wavelength (visible light, infrared etc.) [38]. Only laser sources related to this specific work are presented here, those being the excimer laser and the Nd:YAG laser.

Excimer lasers use mixtures of gases such as Kr and F or Ar and F as the medium with which the laser pulse is created. Excimers are molecules that contain two atoms that are chemically bonded to each other equally, and the bonding occurs only when both atoms are in an excited state. A discharge in a tube that contains the two gas species and a buffer gas creates excimers in the tube. The atoms transition from the excited states that allow them to remain as an excimer to other states, resulting in their mutual repulsion and subsequent separation. The energy difference between the excimer state and the independent states of the atoms is emitted as a photon. Therefore, the elements used as the parts of the excimer affect the energy of the emitted photon. Excimer lasers are often used in UV lithography in material structuring and in labeling of products such as silicon chips and polymers. [43]

Neodymium-doped yttrium aluminium garnet lasers (Nd: YAG) use the energy levels of Nd^{3+} ions. The energy difference of the specific energy levels involved in the laser production results in the emission of a photon with a wavelength of 1064 nm. Nd:YAG lasers are used in material processing, such as drilling, welding, and marking, and in surgery procedures such as eye surgery. [43]

3.5 LIBS spectrometers

Multiple types of spectrometers can be used in LIBS setups, depending on the desired resolution, range, and accuracy of the setup. The three main types of spectrometers are Czerny-Turner, echelle, and Paschen-Runge. Czerny-Turner spectrometers use a setup of two concave mirrors, a grating and a microchannel plate to process the incoming polychromatic light. The mirrors are used to align the light and the grating between the mirrors splits the light into monochromatic light segments which can then be converted into a stream of electrons by the microchannel plate and the electrons will then be detected by a detector. The simplicity of this configuration has made it the most widely used

spectrometer type for LIBS. The limiting factor of a Czerny-Turner spectrometer is the narrow detection range. At once, only about 10-30 nm long segment of the spectrum can be detected. [40]

Echelle spectrometers offer wider spectral region measurements than Czerny-Turner spectrometers, with the addition of high spectral resolution. They use multiple prisms and a special groove grating called echelle grating to split the spectrum into multiple parts. This enables the spectrum to be detected in a square-shaped detector by arranging the narrow-line parts of the spectrum into a square shape. [44]

Another choice for larger spectral region and high spectral resolution is a Paschen-Runge spectrometer. In addition to these benefits, Paschen-Runge spectrometers allow the tuning of detector sensitivity and gating parameters for each spectral line individually. These spectrometers use a curved grating plate positioned on the perimeter of a Rowland circle. Incoming light enters through a slit that is also on the same circle perimeter, and the grating diffracts light into multiple separate exit slits (also on the same circle perimeter). Each exit slit has a photomultiplier tube tuned to best suit the spectral lines arriving at its corresponding exit slit. [40]

3.6 LIBS detectors

Photomultiplier tubes (PMT) and microchannel plates (MCP) convert the incident light into electrons and multiply the electron current into detectable signals. PMTs are nowadays largely used only with Paschen-Runge spectrometers, for they have been replaced by charge-coupled devices (CCD). The main reasons for their inferiority in other spectrometer configurations are their relatively large size compared to CCDs and the fact that they are single-channel only detectors. This means that multiple PMTs are required to detect more than one analyte line at the same time. [41]

A two-dimensional detector array of single photosensitive elements is called a charge-coupled device (CCD). As an incident photon causes free electrons to appear in the detector, the pack of electrons is then transferred to the nearest collection site (a pixel). From the pixels the signal is transferred to the edge of the detector array in a line and then each of these lines is led into an amplifier that creates a corresponding digital output for the signals from each individual packet. [39, 40]

Each element of the array acts as a separate channel in a CCD, which means that CCDs are multichannel detectors. This, along with the fact that CCDs are two-dimensional arrays, allows them to measure multiple spectra at the same time, making it very suitable

for use with echelle spectrometers. [39]

Combining a CCD and a microchannel plate (MCP) creates a device that is often referred to as intensified CCD (ICCD). The incident photons are collected at the photocathode placed at the front of the detector and converted to individual electrons. The electrons pass through the MCP placed behind the photocathode. As these electrons are accelerated with an electric field through the narrow holes of the MCP, they collide with the edges of the holes and generate even more free electrons. The resulting groups of electrons, possibly multiplied by over one million, exit the MCP and collide with a phosphor screen between it and the CCD. The electrons interact with the screen and generate photons, which interact with the CCD. Therefore, the signal of an incident photon from an ICCD is much stronger than that from a plain CCD with the original number of incident photons. [40, 41]

4 Methods and materials

4.1 XRF setups

Different sets of measurements were performed to answer several research questions. Acceleration voltage, filament current and the duration of a single measurement were changed in different measurement sets to determine their effects on the measurement data. Two of each, X-ray tubes and detectors, were used in the measurements to figure out the effect the equipment had on the data. After adjusting the parameters and equipment, I performed the final sets of measurements with the settings that I deemed best for the purposes of each specific measurement.

The acceleration voltage limits the maximum energy of the incident X-rays and it can play an important role in the measurements. A characteristic peak having higher energy than the maximum kinetic energy of the incident X-rays can not be present in the measured spectrum. Therefore, the K-peaks of high-Z elements are not detectable when X-ray tubes with a low maximum acceleration voltage are used. However, these elements can be identified with the lower energy L- and M-peaks, provided that the maximum incident X-ray energy is higher than the energies of these peaks.

The filament current affects the rate of which X-ray photons are produced in the X-ray tube. That, in turn, affects the amount of photons arriving to the detector in a certain amount of time. The measurement time affects how many photons are detected overall, so these variables are closely connected. For example, if the measurement time is reduced by half but the filament current is doubled, the total number of photons detected overall remains the same. In other words, if the measurement time needs to be reduced without a noticeable effect on the number of photons detected, then the filament current needs to be increased accordingly. The maximum input count rate of the detector needs to be taken into account though, so there is an upper limit to how much photons the detector can detect at any given time.

For the XRF measurements, I used two different device setups. The X-ray tomography laboratory of the University of Jyväskylä supplied the measurement location and equipment for the first setup. The source of the X-rays was a 150 kV Microfocus X-ray source L12161-

07 by Hamamatsu and the two detectors used were an XR-100 CdTe detector by Amptek and a FAST SDD attached to X-123 by Amptek. This source was chosen for the initial measurements because of its maximum acceleration voltage of 150 kV which allowed me to detect the Kα peaks of heavier metals such as tungsten and rhodium. Because this X-ray source is mainly used for tomography imaging, its X-ray beam had to be narrowed down to interact only with the samples. For this purpose, a 5mm thick sheet of lead was inserted between the source and the sample holder. The detector was placed at a 45-degree angle relative to the incident beam. A photo of the measurement setup and a geometric presentation can be seen in Figure 15. The sample position on the sample holder was determined with a fluorescent plate that showed the area where the X-rays were traversing at the sample distance from the source and the lead plate. I measured the samples with this setup for approximately 1 minute of irradiation at a time and saved the spectra for later analysis. The measurements included two different acceleration voltages, 50 and 70 kV. Both detectors were used at the same time to make their comparisons easier.

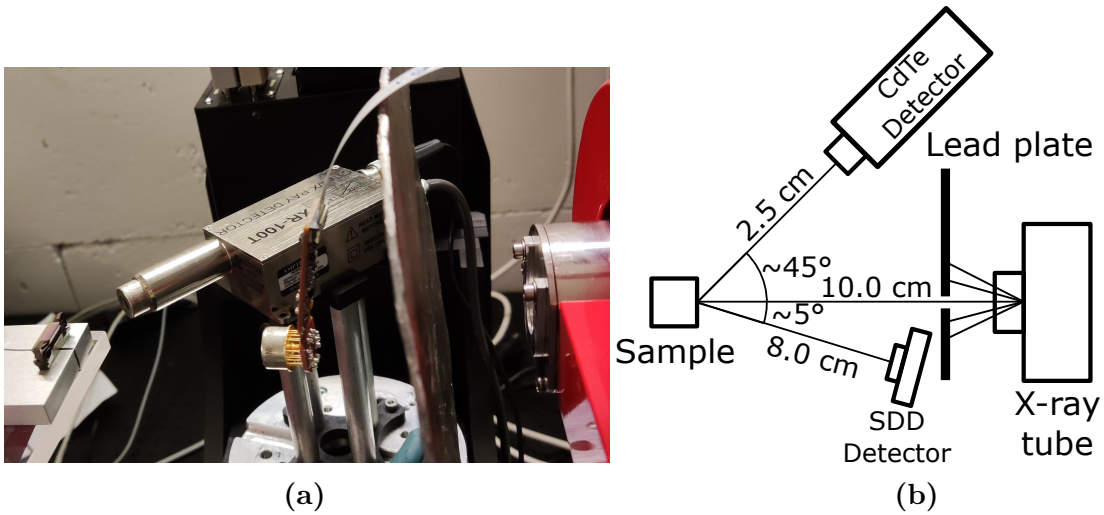

Figure 15. Measurement setup 1 (see Table 1): a) photo of the actual setup and b) concept figure of the setup.

I built the second measurement setup for XRF in a lead-lined measurement station. As an X-ray source I used packaged X-ray tube FM-33 by Micro X-ray Inc. and the only detector I used was the same FAST SDD/X-123 detector. A photo of the setup and a concept image are presented in Figure 16. A Spellman uX50P50 was used as the high-voltage source for the X-ray tube. The tube was collimated with a 50 mm long brass collimator with a hole of 1 mm diameter.

Table 1. XRF setups and the parameters common to all measurements made with the respective setup.

Setup	1	2
X-ray tube	Hamamatsu	Micro X-ray
Acceleration voltage (kV)	50 and 100	50
Filament current (mA)	0.1	1
Detector	CdTe and SDD	SDD
Detector channels	2048	2048
Peaking time	4.0 µs	4.0 µs

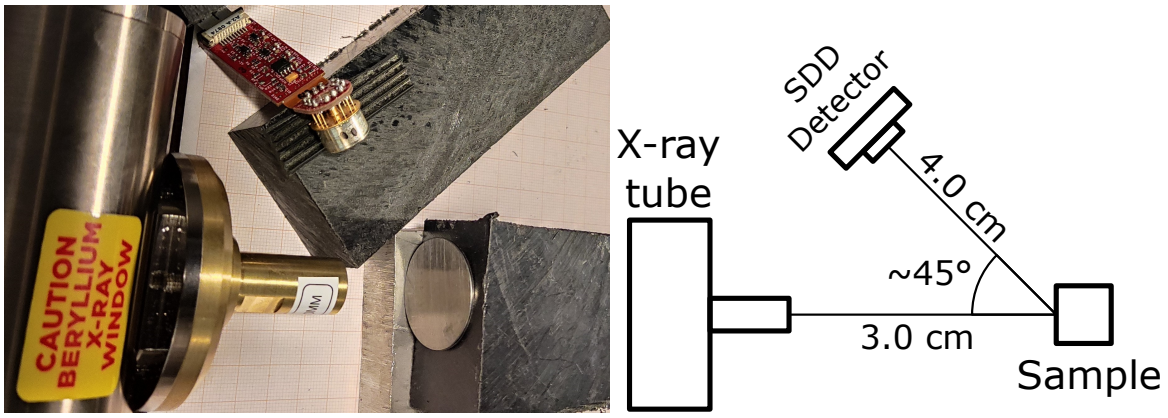

(a) **(b)**

Figure 16. Measurement setup 2 (see Table 1): a) photo of the actual setup and b) concept figure of the setup.

4.2 Energy calibrations of the X-ray detectors

In order to identify the characteristic peaks of elements, the measured spectra needed to be calibrated. I did this by assigning characteristic energy values for the most prominent peaks in the spectra. These values I gained from X-Ray Data Booklet [45]. The samples used for the calibration were a steel reference SRM 1157 by NIST [46] and a copper shutter of the Hamamatsu X-ray source.

I did the calibration of the CdTe-detector with the setup of Figure 15. The X-ray source I used was the Hamamatsu, and the acceleration voltage was 70 kV. The peaks I chose for the calibration purposes were those of copper, tungsten, iron, and molybdenum (see Figure 17a). I assigned the corresponding channels with these energy values, and on the basis of those I performed the calibration with the PyMCA software. The calibration equation is of second order and the parameter values can be seen in Table 2 in the first column.

I did two separate calibrations for the SDD-detector because of slight variation in the channels corresponding to characteristic peaks. The variation is most likely the result of the difference in temperature of the detector element between different measurements. The peaks I used for these calibrations were those of molybdenum, iron, and argon, and the X-ray source was Hamamatsu with the acceleration voltage of 70 kV (see Figure 17b). In addition to those peaks, I used the peaks of rhodium caused by the rhodium target in the calibration done with the Micro X-ray Inc. X-ray tube with 50 kV acceleration voltage (see Figure 17c). These calibrations are also of second order and the parameters are tabulated in the second and third columns of Table 2.

Table 2. Calibration parameters of the XRF measurement setups. Calibration equation: $A + Bx + Cx^2$

	CdTe1	SDD1	SDD2
A	-0.1217	0.0175	-0.0745
B	0.0603	0.0151	0.0156
C	$0.1607 \cdot 10^{-7}$	$1.248 \cdot 10^{-7}$	$-1.200 \cdot 10^{-7}$

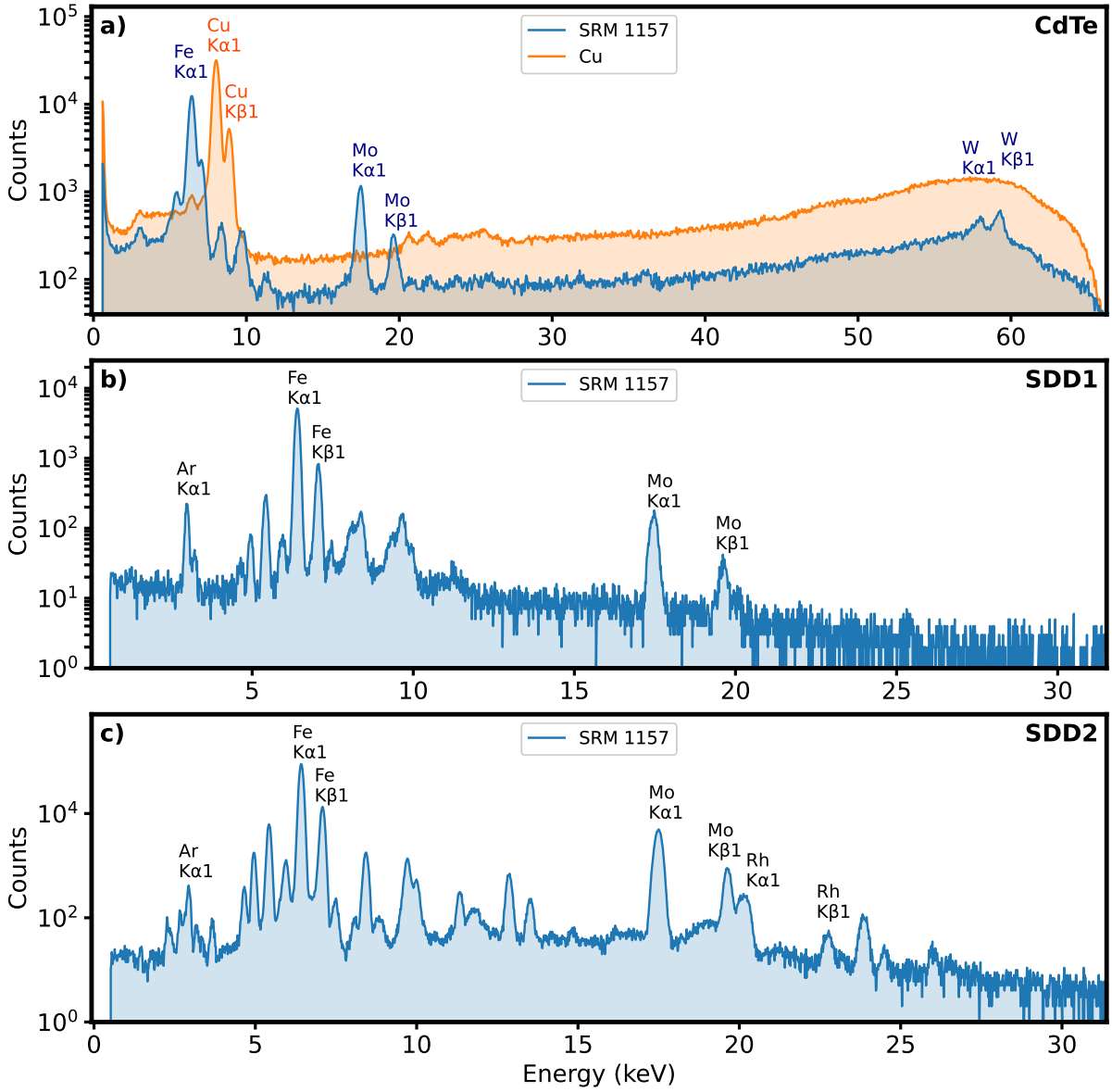

Figure 17. The spectra used for calibrations of the detectors. The peaks marked to the figures were used for the calibration of the energy axis. The peaks of spectra in a) were used for the calibration CdTe1, and the spectra in b) and c) were used for the calibrations SDD1 and SDD2, respectively. The energy axes in the figures were positioned according to these calibrations.

4.3 LIBS setups

I performed the LIBS measurements at two different locations: in Nanoscience Center of the University of Jyväskylä and the laboratory of the applied optics group of Tampere University in Hervanta, Tampere. I did this to gain more information by using multiple measurement setups and to determine how the setups in question affect the measurements. The most important parameters in these measurements were laser pulse energy, laser pulse duration, the number of total laser pulses per measurement, and the timing of the detection of plasma spectrum.

The energy of the laser pulse determines the amount of material it can ablate from the sample surface. Therefore, it is a very central parameter with the focusing of the laser at the surface when the goal is to ablate the possible coating from the surface of the sample to gain optical access to the bulk of the sample. In addition to this, it also affects the size of the plasma formed from the sample which intensifies the detected spectrum.

The duration of the laser pulse determines whether the entire energy of the pulse reaches the sample or not. The forming of plasma cloud can disrupt the tail of the pulse from reaching the sample and result in the absorption of pulse energy by the plasma cloud. This can prolong the time it takes for the plasma to cool down sufficiently for the measurement of discrete spectrum.

The number of laser pulses affects the depth of the crater formed in the sample. As the number of pulses increases, the crater deepens and the measured spectrum loses its intensity and becomes all the more flatter. This is due to the effect the crater edges have on the pulse, as the pulse is partially obstructed when reaching the bottom, and the obstruction of plasma formation and expansion.

The timing of the spectrum detection is of paramount importance to the quality of the spectrum. It needs to be measured as the plasma has cooled and expanded enough so it emits a discrete spectrum instead of a continuous one but before it has dissipated too much. The length of the detection affects spectrum intensity and quality as well.

In addition to the parameters mentioned above also the fact that the laser should be focused at the surface of the sample means that the samples must be positioned correctly before the measurements. This is relatively simple when measuring single samples independently, since just the front of the sample needs to be aligned to the focal length of the laser. However, as the sample surface is cratered at the position of the focal point of the laser, the exposed material is not at the focal length of the laser anymore and,

therefore, the laser is not as powerful as in full focus on the surface. This is a fact which presents a challenge when contemplating in-line applications for samples of different sizes.

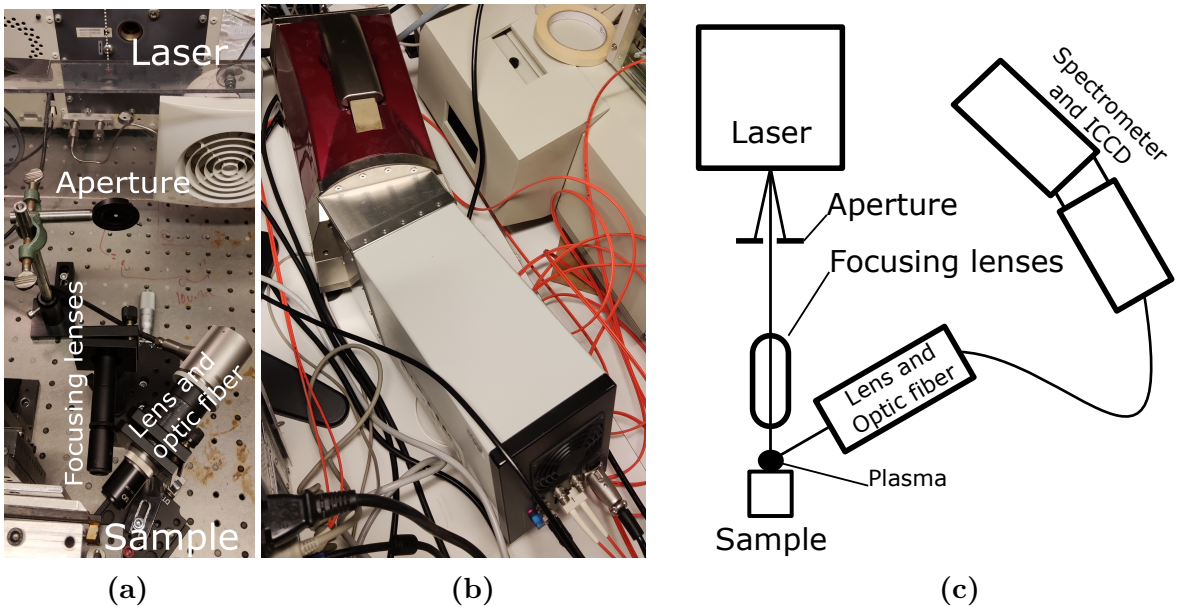

(a) **(b)** **(c)**

Figure 18. Measurement setup in the Nanoscience Center in University of Jyväskylä: a) photo of the lenses and sample holder, b) photo of the spectrometer and the detector, and c) concept figure of the whole setup.

The measurement setup in Nanoscience Center is presented in Figure 18. It consists of an Optex ArF excimer laser by Lambda Physik, focusing lens system, sample holder, spectrum collection lens system, a Mechelle 7500 spectrometer by Multichannel Instruments with an integrated DiCAM PRO ICCD camera. I performed the measurements with the supervision of Heikki Häkkänen and Saara Kaski, both of whom have a lot of experience in LIBS measurements. The parameters of these measurements are listed in the first column of Table 3. These measurements consisted of 40 consecutive laser pulses fired at each sample in turn. Plasma spectra were measured after each pulse with a delay of 1 µs. This delay was tested to be suitable for WC-Co samples before the actual measurements. The range of the spectrometer was wide enough to allow for the simultaneous measurement of both wavelength regions shown in Figure 23, namely 355 to 365 nm and 424 to 431 nm.

For the other measurement setup, Mikko Laitinen and I visited the laboratory of the applied optics group in Tampere University. Figure 19 presents this setup. It included a Quantel Ultra (50-100 mJ) as the laser, a sample holder, a lens system for focusing the laser pulse and for the collection of the plasma spectrum, and an Andor Kymera 328i spectrometer by Oxford Instruments with an Andor iStar 334T ICCD camera. The

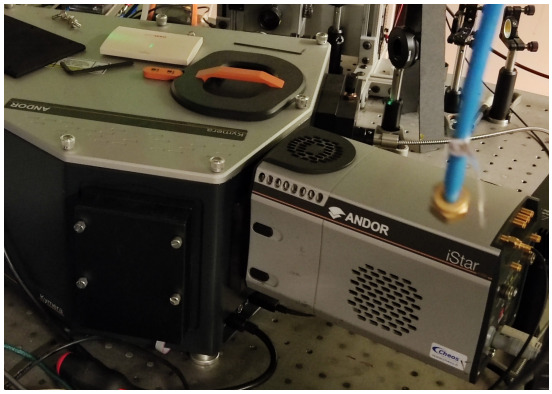

(a)

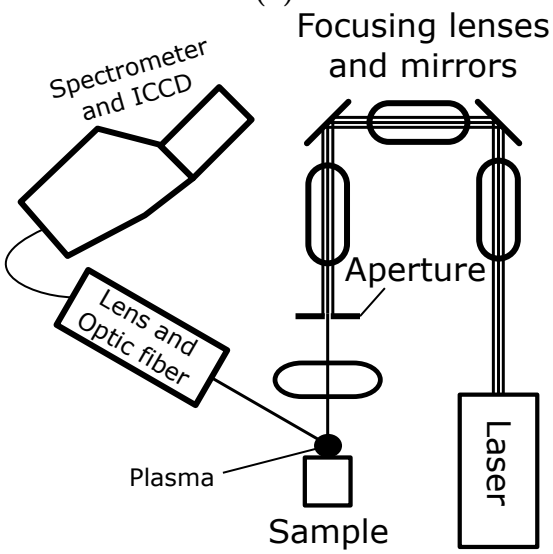

(b)

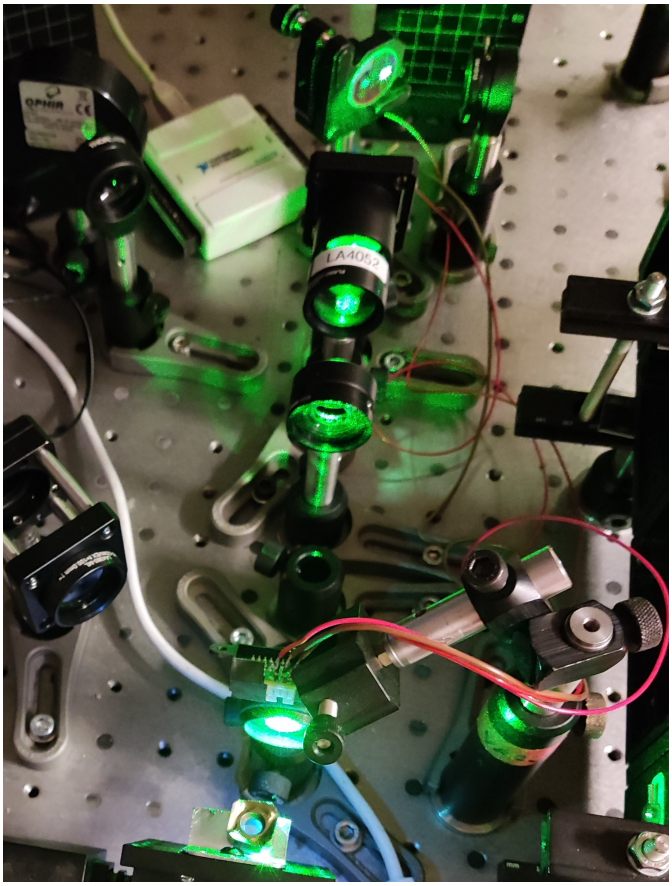

(c)

Figure 19. Measurement setup at Tampere University, a) photo of the spectrometer and the detector, b) concept figure of the setup as a whole, and c) photo of the lenses and the sample holder.

Table 3. Parameters and equipment details for both of the LIBS measurement setups. The first column is from the measurements at Jyväskylä and the second from those at Tampere.

Setup	1	2
Laser	Optex (Lambda Physik)	Ultra (50-100 mJ) (Quantel)
Type	ArF excimer	Lamp pumped solid state
Wavelength	193 nm	1064 nm
Laser energy	6 mJ	4-27 mJ (11.25 mJ)
Pulse Frequency	5 Hz	20 Hz
Pulse Length	1000 ns	6 ns
Delay	1.0 µs	0.2-3.0 µs (1.0 µs)
Spectrometer	Mechelle 7500 (Multichannel Instruments)	Kymera 328i (Oxford Instruments Andor)
ICCD	DiCAM PRO	iStar 334T (Oxford Instruments Andor)

collection lens system was filtered to prevent the reflected incident laser light (1064 nm) from damaging the spectrometer and the detector. I performed the measurements with the help and guidance of Juha Toivonen and Joni Ahokas, since Juha has a wide knowledge of LIBS measurements, and Joni was accustomed to this particular measurement setup by measurements of his own. The parameters for these measurements are listed at the second column of Table 3. First I adjusted and measured the laser energy and delay to determine the most suitable values for the actual measurements of the samples and to analyse their effect on the spectra. I chose to set the delay to 1 µs based on the new delay measurements I performed. After calibration measurements and fine tuning of the parameters, I measured the samples with 50 laser pulses and the total spectrum of these pulses were recorded. This was done with the laser energy set to 11.25 mJ. In addition to that I measured the depth profiles of three samples after one, two, four, ten, and twenty laser pulses. Also, for the sample with the highest Cr content, sample 13, I did a more specific depth profiling. This included twenty laser pulses, and the plasma spectrum was measured after each pulse. For the depth profiling the laser energy was increased to 27 mJ.

Due to the preset use settings of the setup at Tampere, acquisition of a single spectrum from a series of pulses after each pulse was a time consuming process. Each pulse had to be fired manually and the spectrum saved independently. Since only one day had been reserved for my measurements in Tampere and the preparations and parameter adjustments took some time, I was able to measure the pulse by pulse depth profile of 20

pulses only for sample 13, the sample which had the highest chromium content according to the reference data by Tikomet.

In addition to the WC-Co samples I also measured pieces of pure elemental metals for reference and to see how well their spectral peaks are present without the interference of other elements. The most important metal I measured was chromium to verify that the spectral peaks of Cr were visible with each setup and to make sure that the calibration of the detectors were correct, or at least very near correct so it could easily be corrected during analysis of the results.

The choice to perform LIBS measurements in both locations originated from the interest of having results from more than one setup to compare and gain advantage of the differences of these setups. The difference in laser type (gas in Jyväskylä and solid state in Tampere) and the fine tuning of the setups was different and so they provided me with a good opportunity to focus on different options in measurements. For example, in Tampere it was possible to get statistics on how the energy of the laser pulse and the delay before the measurement of the plasma spectrum affect the collected spectrum. On the other hand, in Jyväskylä it was possible for me to familiarise myself with the LIBS setup and to perform multiple sets of measurements to the samples.

4.4 Calibration and adjustment of LIBS setups

I looked up the positions and intensities of atomic emission lines from NIST Atomic Spectra Database [47] and used those values for the calibration and analysis of the spectra. Measurement setup 1 in Jyväskylä had a detector which had internal calibration that seemed to be accurate enough, so it did not require any additional calibration actions. However, data from setup 2 in Tampere needed to be calibrated during data analysis because there was a slight offset visible at the position of the peaks when measuring a piece of reference Cr. The offset correction was done by taking an average of the distances between the positions of the three peaks in the data and the actual positions from literature. Figure 20 presents this offset and how it affected the peak position in the measurements.

Setup 2 in Tampere had simple variability settings in the laser energy and the delay of measurement of the plasma spectrum, so their effect on the spectra was investigated as well. Figure 14a shows multiple spectra from a piece of Cr measured otherwise identically but for the measurement delay. A sweet spot for the delay was determined by varying the delay between 0 and 3 µs, with the best delay turning out to be 1.0 µs. This is represented by the black line in Figure 14a. It shows the best contrast between the high points in

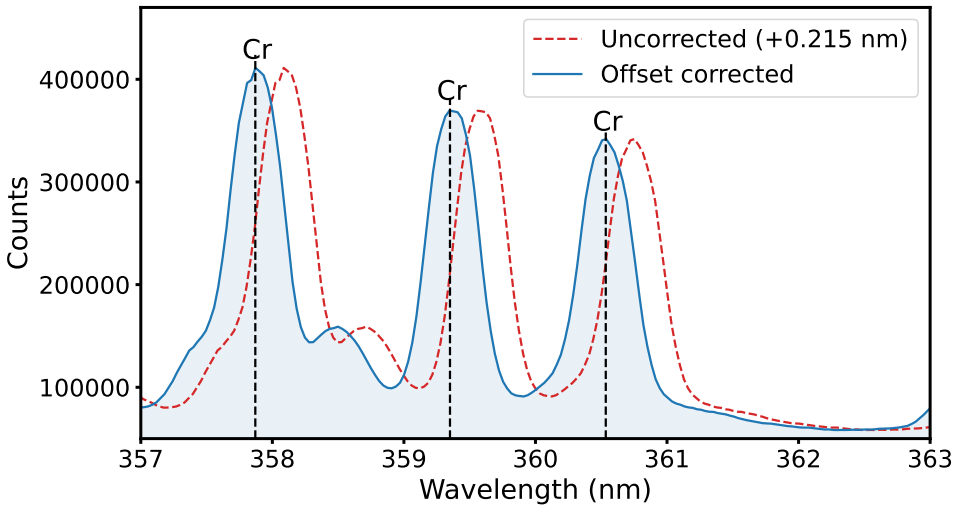

Figure 20. Offset correction for the spectra measured with the LIBS setup in Tampere University. The sample used for the correction was a piece of elementally pure (> 99 %)chromium.

the peaks and the low points in the valleys of the spectra and thus is optimal for the detection of peaks from the background of these spectra. Figure 14b presents spectra from an arbitrary sample with different energies, ranging from 4.25 mJ to 27.00 mJ per pulse. In these spectra there is not an overly large difference in the contrast between peaks and background. 11.25 mJ energy was used in some of the measurements since it provided margin to increase the energy if needed, but it would not be too high an energy to make the crater too deep too fast. In the depth analysis measurements 27.00 mJ energy was used to gain good crater formation.

4.5 Samples

Samples for this work were provided by Tikomet company. Tikomet also provided the high power XRF element analysis data from the samples for reference use. This data is tabulated in Table 4. Figure 21 presents four arbitrary scrap pieces as an example of the sample size and geometry. Nine out of thirteen samples were WC-Co samples that contained more than 70 mass% tungsten and around 8 mass% cobalt and the other four were different types of steel, ceramic metal, and alumina. The different samples provided a clear perspective as to how WC-Co spectra differ from those of other materials.

Table 4. XRF reference data provided by Tikomet, the numbers are mass percentage values. The column containing percentages of chromium is marked with green and samples that are not WC-Co hardmetals are marked with yellow.

Sample	Notes	Cr	W	Co	Ti	Ta	Fe	Nb	V	Ni
3		0.00	> 70	< 8	< 1	> 1	< 0.2	< 1	< 0.2	< 0.2
5		0.00	> 70	> 8	< 1	< 1	< 0.2	< 1	< 0.2	> 0.2
7		0.19	> 70	> 8	> 1	> 1	< 0.2	> 1	< 0.2	< 0.2
8		0.00	> 70	< 8	< 1	> 1	< 0.2	< 1	< 0.2	< 0.2
9		0.00	> 70	> 8	< 1	< 1	< 0.2	< 1	< 0.2	< 0.2
13		0.45	> 70	> 8	< 1	< 1	> 0.2	<1	< 0.2	> 0.2
14		0.00	> 70	< 8	< 1	< 1	< 0.2	< 1	< 0.2	< 0.2
16		0.00	> 70	> 8	> 1	> 1	< 0.2	> 1	< 0.2	> 0.2
18		0.00	> 70	> 8	> 1	$\gg 1$	< 0.2	> 1	< 0.2	< 0.2
19	TiC Alumina	0.00	$\ll 70$	< 8	$\gg 1$	< 1	< 0.2	> 1	> 0.2	> 0.2
20	HSS	5.29	$\ll 70$	< 8	< 1	< 1	$\gg 0.2$	< 1	$\gg 0.2$	< 0.2
21	Cermet	0.93	$\ll 70$	< 8	$\gg 1$	< 1	< 0.2	> 1	> 0.2	$\gg 0.2$
22	Alumina	0.16	$\ll 70$	< 8	< 1	< 1	< 0.2	< 1	> 0.2	< 0.2

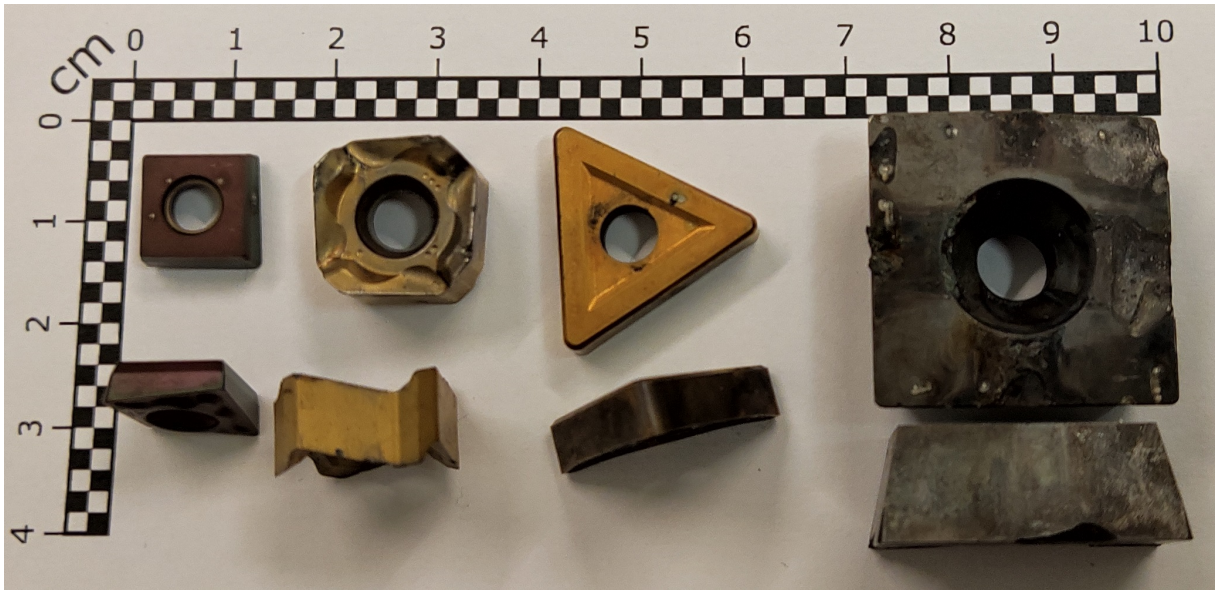

Figure 21. Four arbitrary example scrap pieces provided by Tikomet. Top and side views from each sample with a length scale in centimetres for reference. Sample numbers from left to right: 7, 13, 14 and 16. The spots visible in the pieces in the top row are the craters caused by LIBS measurements.

4.6 Data analysis

I did the data analysis of the measured spectra with Python and Python-based programs. The XRF spectra were calibrated and processed with PyMca-software [48]. This software was a very useful tool in the calibration step and in visualising the spectra before I had made any scripts of my own. I performed the data analysis of the spectra with my own Python scripts using matplotlib and numpy libraries.

5 Results and discussion

5.1 Example XRF and LIBS spectra

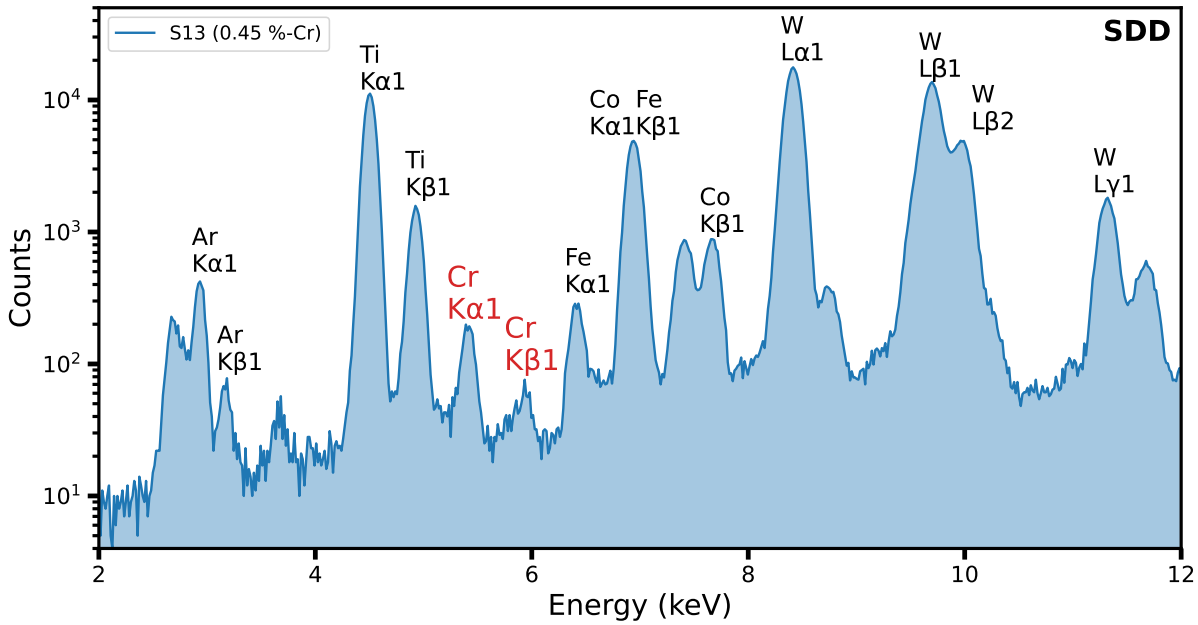

Figure 22. An example XRF spectrum of a WC-Co sample 13 which contains 0.45 % chromium. The peaks corresponding to certain elements are labelled with their respective characteristic X-ray notations. Notations for Cr peaks are highlighted red. The setup used for this spectrum was SDD2.

In order to demonstrate what this work is about, it is worthwhile to show some examples of what the XRF and LIBS spectra actually look like and what information they contain. Figure 22 presents an example XRF spectrum from the sample 13 measured with the XRF setup 2. The elements that cause peaks in the spectrum are marked in the vicinity of the corresponding peak. For example, the peaks labelled W Lα1, W Lβ1, and W Lγ1 are the result of the presence of tungsten (W) in the sample. However, elements not present in the sample but present in the measurement environment can also create peaks in the spectrum. A good example of this is the presence of peaks labelled Ar Kα1 and Ar Kβ1. The air surrounding the measurement setup contains a small amount of argon (Ar) which appears in the spectrum. The most important peaks regarding this work are those created

by chromium (Cr) present in the sample. Those can be seen in Figure 22 as the peaks labelled Cr Kα1 and Cr Kβ1. Sample (13) contains approximately 0.45 % chromium according to the reference data provided by Tikomet (see Table 4).

Figure 23 shows an example of a LIBS spectrum. This spectrum is from a chromium metal sample so it presents the Cr emission peaks clearly. It serves to show the positions of clear Cr peaks without the interference of other elements. According to the NIST reference data [47] these were the most prominent peaks to look for in the spectra of the samples and also to determine if there are peaks caused by other elements in these positions. Especially these two sets of three peaks at two different wavelength areas were focused on in the analysis since they are relatively intense peaks.

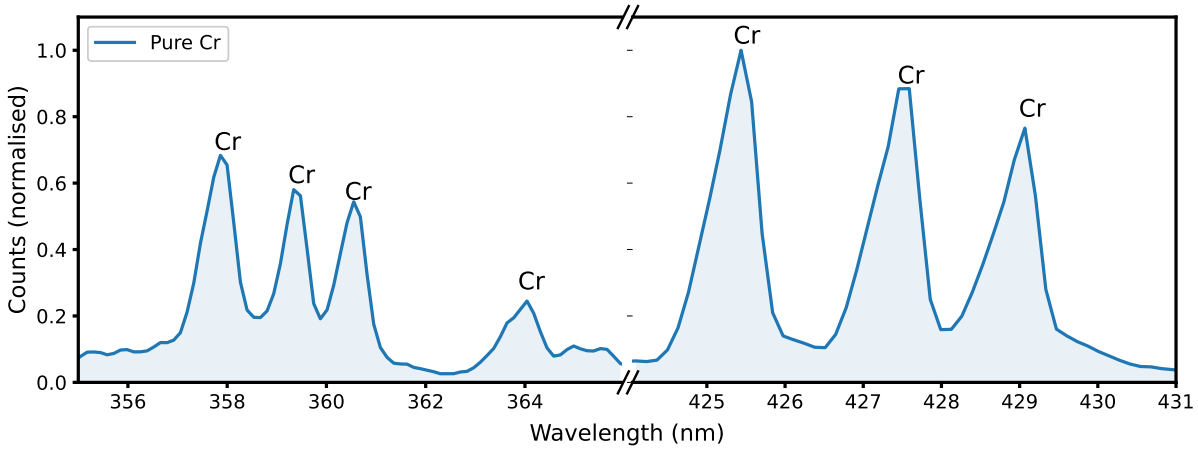

Figure 23. An example LIBS spectrum of a piece of Cr metal with clear Cr emission peaks visible in it. These peak positions were analysed from the samples.

5.2 XRF analysis of Cr from WC-Co

Figure 24a shows the spectra of two samples measured with the measurement setup 1, those samples being the ones with with Cr contents of 0.45 and 0.00 %,respectively, with acceleration voltages of 50 and 70 kV. The detector used to obtain these spectra was the CdTe detector. Figure 24b presents a zoomed-in view of the spectra. The CdTe-detector has a wide measurement range and is able to detect K peaks of tungsten near 60 keV. However, it does not have high enough resolution to show sharp Cr peaks, partially due to high incident X-ray energy. In the 50 kV spectra a peak is present in the Cr Kα energy for both samples. However, for the 0.00 % sample, the peak is very small and has a bit higher energy than the Cr Kα energy, so it is likely caused by something else than chromium.

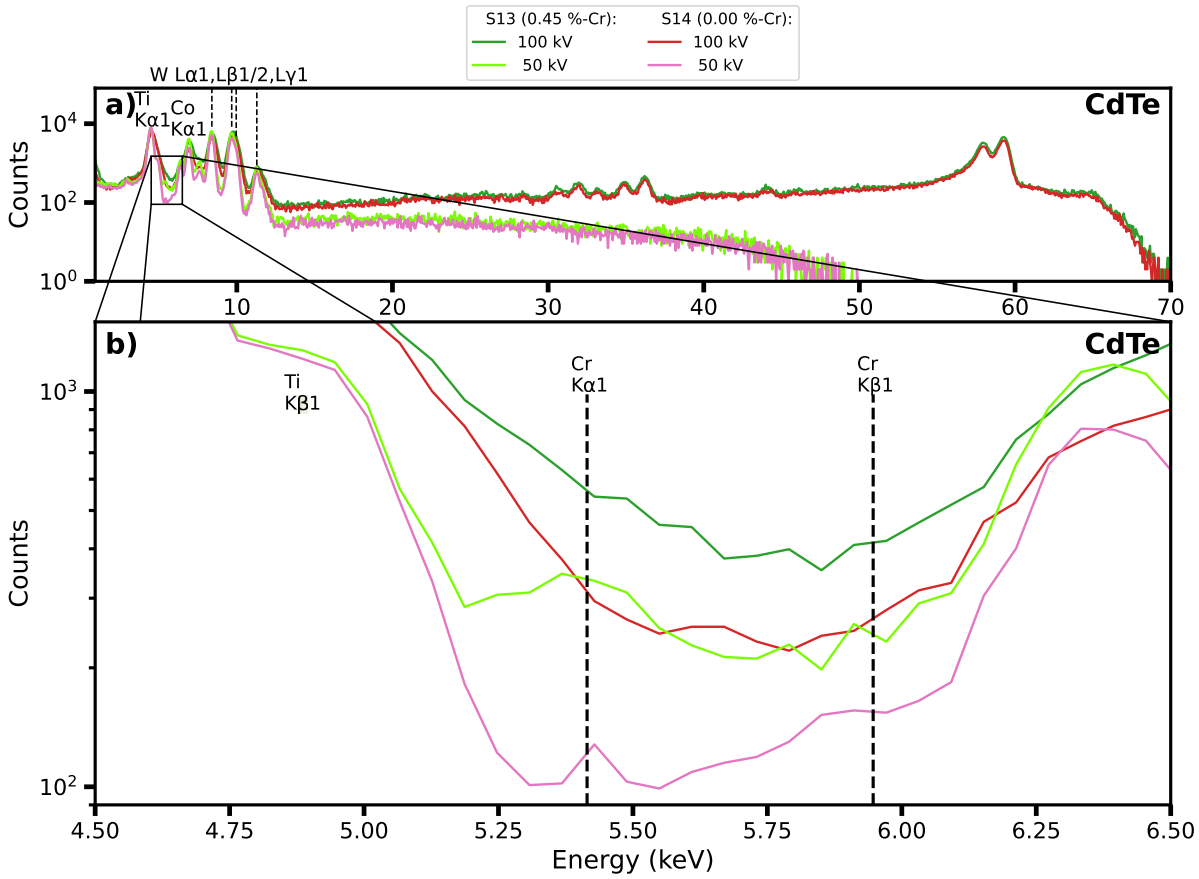

Figure 24. XRF spectra from samples 13 and 14 with Cr contents of 0.45 % and 0.00 %, respectively, measured with measurement setup 1. The samples were measured with two different acceleration voltages, 50 kV and 70 kV. Figure a) shows the whole spectra and b) is a zoomed-in view of them. The detector used was CdTe detector. Wide Kα peak of Cr is visible in 50 kV high-Cr spectrum but not in 70 kV spectrum. The bremsstrahlung of the X-ray tube and the resolution of the detector cause the Cr peak to disappear into the background.

When the acceleration voltage is increased to 70 kV, the peaks near the Cr Kα energy are not present in the spectra. The spectra appear very smooth, since most of the channels have at least a few dozen counts. The resolution of CdTe detector at 5 keV range is not sufficient for Cr quantification from the spectra.

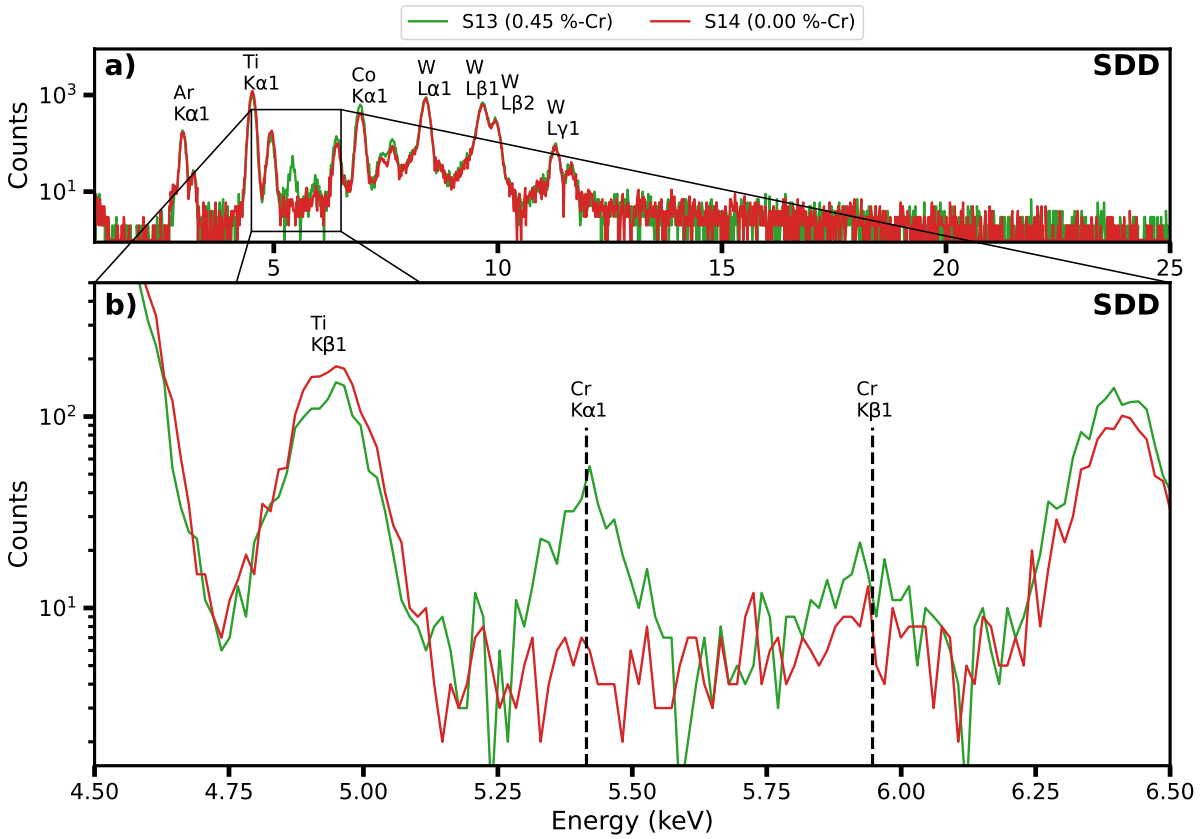

Figure 25. Spectra of samples 13 (0.45 %) and 14 (0.00 %). The spectra were measured with XRF measurement setup 1 with SDD as the detector and acceleration voltage of 50 kV. a) shows the whole spectra and b) is a close-up around the energy of the Cr K peaks. The Cr Kα peak can be seen clearly over the background in the high-Cr sample spectra and not at all in the low-Cr sample spectra.

Figure 25 shows the same measurement as in Figure 24 with measurement setup 1 and acceleration voltage of 50 kV with the exception that the detector used was the SDD. The energy range of this detector is smaller than the range of the CdTe detector but the resolution of SDD is better than in CdTe. This is evident when comparing the number of distinct peaks between 0 and 15 keV in the CdTe spectra and the SDD spectra: the SDD spectra has about double the number of peaks in this area. The spectra are nearly identical everywhere except near Cr Kα peak energy, indicating that the samples resemble each other in elemental composition, with Cr content excluded. Kα peak of Cr is clearly

visible in the high-Cr sample and absent in the non-Cr sample. This indicates that the SDD could be useful in comparing the height and shape of the spectra in an area around Cr Kα energy as well as Cr Kβ energy. Because the Cr peaks consist only of a few dozen counts, noise has a large effect on the smoothness of the peaks.

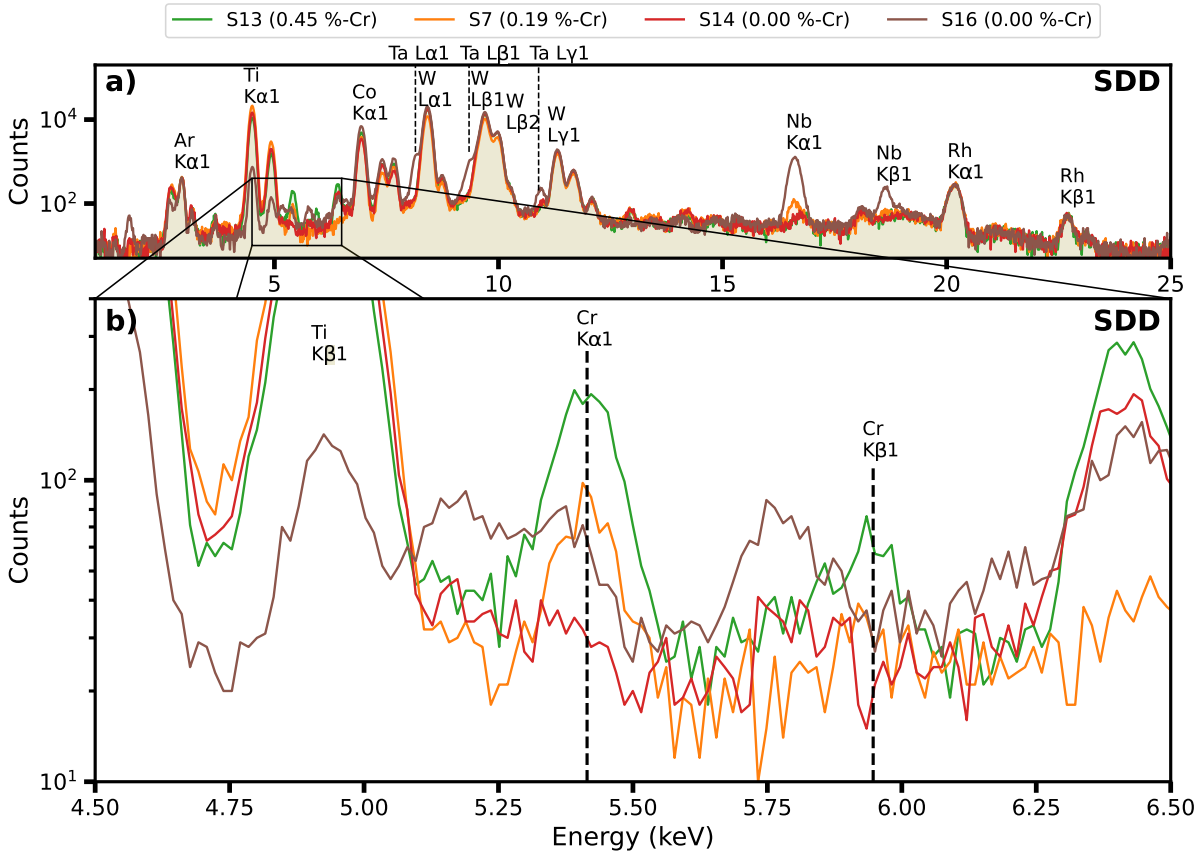

Figure 26. The spectra of 4 different samples measured with measurement setup 2. Figure a) shows the whole spectra of samples 13 (0.45 %), 7 (0.19 %), 14 (0.00 %), and 16 (0.00 %) and Figure b) is a close-up of the spectra. The Cr Kα peaks are clearly distinguishable from both high-Cr sample spectra where as the higher energy Cr Kβ peaks are not. No distinct Cr peaks are present in the non-Cr sample spectra.

Figure 26a presents the spectra gained from four samples by using the measurement set-up 2. The samples had Cr contents as follows: 0.45, 0.19, 0.00, and 0.00 %. Although the other parts of the spectra were mostly very similar to each other, especially the area near Cr Kα energy differed a lot depending on the Cr content of the sample in question. From the close-up of the spectra in 26b it can be seen that the samples which have a high Cr content form a clear peak in the energy corresponding to Cr Kα energy, while the samples without Cr do not. This implies that the appearance of a peak in Cr Kα energy

position can be used to determine whether the sample has a Cr content of at least 0.19 % in the type of samples in question in this work. However, to be certain of the presence of Cr it would be wise to compare the heights of both Cr peaks in the spectra. The count value alone at that position is not a good enough parameter for that determination since, as can be seen in 26b, one of the non-Cr samples has a count value close to that of the second highest Cr content sample at Cr Kα energy position. For this reason, it is useful to perform a fitting of a parabola to the parts of the spectra at the Cr peak energies to identify the peak shapes.

In addition to the spectra of the samples in Figure 26, four other sample spectra were also measured in detail. These were all from samples that did not contain Cr, according to the reference data by Tikomet. The spectra are presented in Figure A1. Some peaking can be interpreted in some of these spectra, but in comparison with spectra of samples containing Cr, there is a difference in the intensity of the peaks.

Based on the spectra presented before it seems that a clear and reliable method of distinguishing Cr contents in these kind of samples is to focus on the presence (or absence) of Cr Kα peak. It forms a distinguishable peak shape in both 0.45 and 0.19 % cases, as can be seen in Figure 26b. Although the spectra of the samples without Cr can be approximately the same intensity as those with Cr in this position, they do not form a peak shape centred in Cr Kα position. The differences in the shapes are large enough that they may be detected by a software designed to process XRF spectra and distinguish clear peaks in it. In the case of similar samples with Cr contents of 0.19 % or more, these results indicate that they are distinguishable from samples that do not contain Cr or contain it in very small amounts. If the expected Cr content of the undesired samples is somewhere between 0.19 and 0.45 % then Cr Kβ peak could possibly be used to ensure the interpretation of whether the sample contains Cr or not.

Exception to the Cr identification would be heavy element coatings thicker than about 1 µm, since Cr Kα photons could not penetrate them easily anymore. However, from the XRF spectra it is possible to determine the elements of the coating and also the thickness by comparing the heights of the peaks. This could be included as a safety procedure in a way that when a sample with high contents of coating elements is measured, it would be grouped with the high Cr content samples as a precaution since it is not easy to determine the actual Cr content of that sample.

5.3 LIBS analysis of Cr from WC-Co

5.3.1 LIBS in University of Jyväskylä

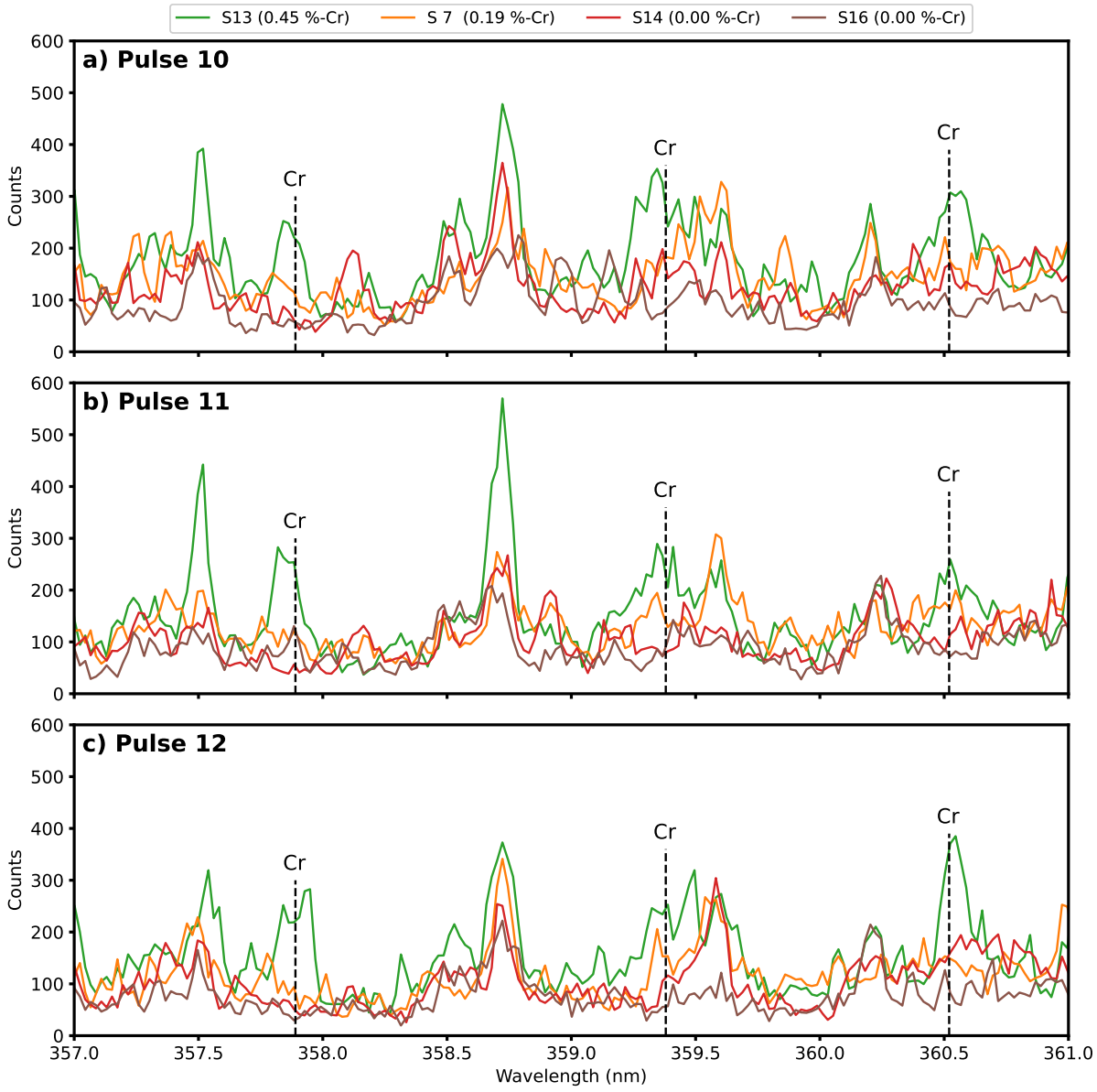

Figure 27. LIBS spectra from three consecutive laser pulses (10^{th}, 11^{th}, and 12^{th}) from samples 13, 7, 14, and 16 between 357 and 361 nm with setup 1.

The measurements done at the University of Jyväskylä were performed with LIBS setup 1 (see Table 3). Figure 27 contains spectra from four samples: 13, 7, 14, and 16. The samples were exposed to multiple consecutive laser pulses and spectra were measured after each pulse. Figures 27a, b, and c were measured after 10^{th}, 11^{th}, and 12^{th} pulse,

respectively. The emission line positions for Cr in Figure 27 are 357.89, 359.38, and 360.52 nm. Each spectral peak position of Cr in this range seems to contain a peak for the sample that has the highest Cr content. However, for the second-highest Cr content sample there does not seem to be a peak that separates it from the samples without Cr. The clearest positions for Cr-related peaks are 357.89 and 360.52 nm but this only applies to the sample with 0.45 % Cr.

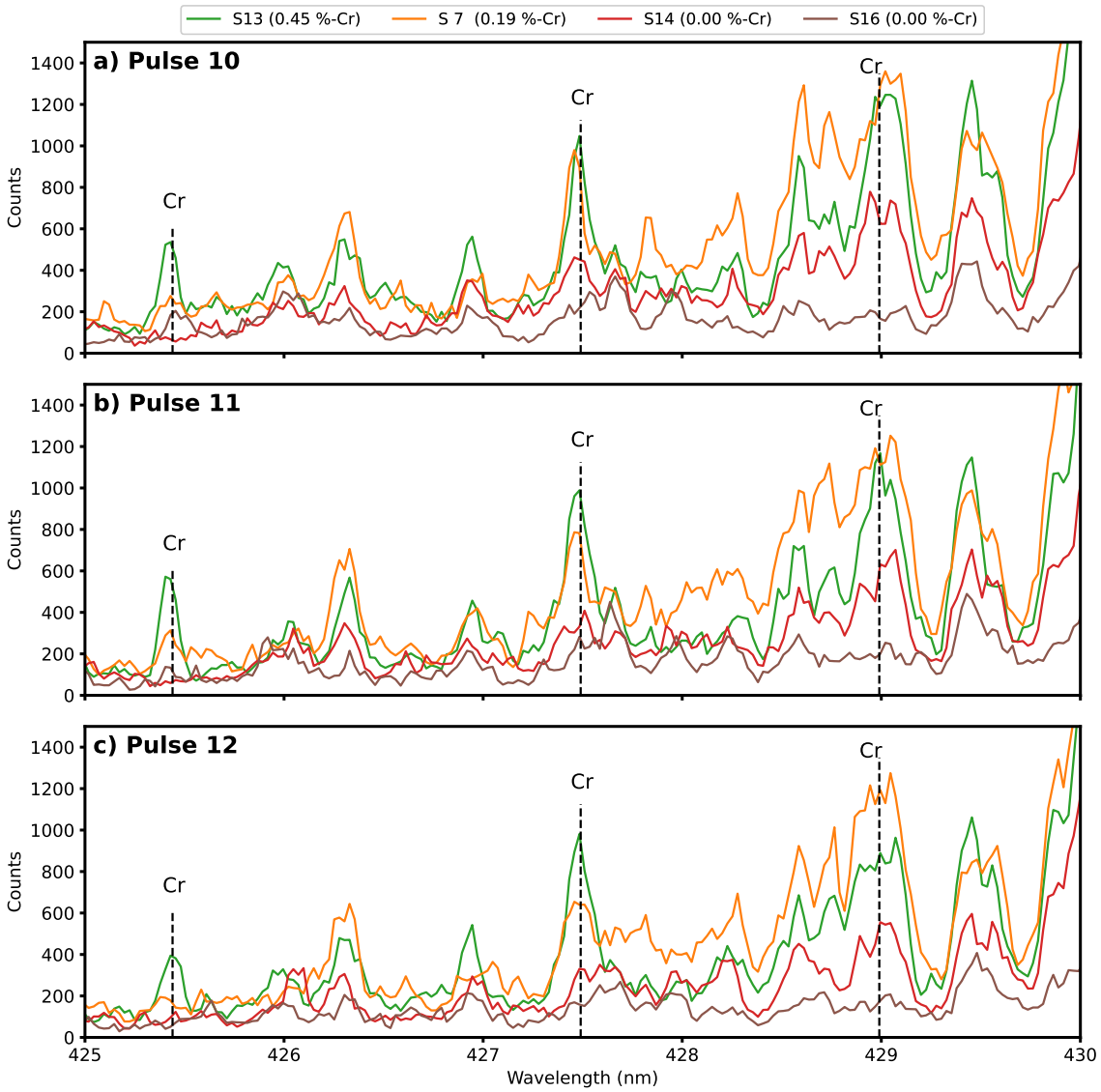

Figure 28. LIBS spectra after three consecutive laser pulses (10^{th}, 11^{th}, and 12^{th}) from samples 13, 7, 14, and 16 between 425 and 430 nm. The spectra were measured with the LIBS setup 1.

Similarly Figure 28 presents the same spectra from same measurements as Figure 27 but in different wavelength range. In this range, the emission line positions for Cr are 425.44, 427.49, and 428.99 nm. Samples that contain Cr have a clear peak in 425.44 and 427.49 nm. In the case of three out of the four spectra shown in Figure 28 there is a peak at 428.99 nm. Since, it is most likely caused by some other element(s) than Cr, and it does not seem as a reliable position for determining the presence of Cr in these samples. The peaks at 427.49 nm might be useful in identifying down to 0.19 % Cr content in the sample. However, as there were only a few sample pieces, this is not at all certain as evidenced by Figure A3.

For both of the wavelength ranges presented above, there also were additional measurements of four samples that do not contain Cr. These spectra are presented in the Appendix A since they provide only additional information from LIBS measurements. However, comparing these with the spectra of samples that contain Cr adds reliability to the analysis of which peaks are caused by Cr and which are not.

Figures 27 and A2 indicate that the three marked spectral peak positions of Cr at 357.89, 359.38, and 360.52 nm appear to be reliable for identifying Cr content of 0.45 % or more. However, the 359.38 nm position has quite a lot of interference caused possibly by nearby spectral peaks of other elements.

When comparing Figure 28 with Figure A3, it is clear that the peak at 428.99 nm is not caused by Cr alone because it exists also in samples that do not contain Cr. Similarly, there is at least a small peak at 427.49 nm in every spectra regardless of the Cr content of the sample. Therefore, 425.44 nm position seems to be the best out of these three positions to determine whether the samples contain Cr.

When the spectra measured after different pulses are summed, they retain the peaks that were already visible in single pulse spectra, as shown in Figure 29. These sum spectra provide a wider window for the laser pulse measurements while still including information about the Cr content of the samples. Since different samples can be ablated by different rates per laser pulse these kinds of sum spectra over a series of pulses may work more reliably in the case of varying multiple coated and uncoated samples.

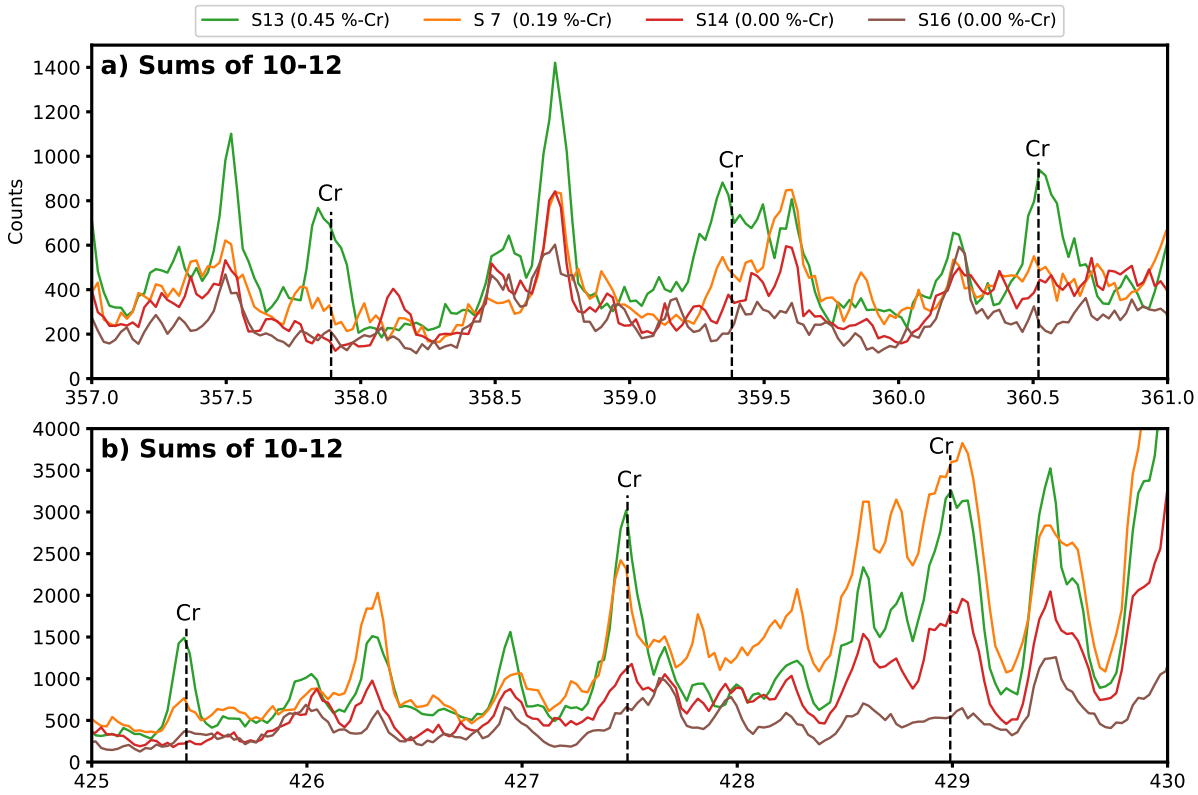

Figure 29. The sum spectra of LIBS measurements after three consecutive laser pulses (10^{th}, 11^{th}, and 12^{th}) from samples 13, 7, 14, and 16. Figure a) shows the sum spectra in the range between 357 and 361 nm, and b) the same spectra between 425 and 430 nm.

5.3.2 LIBS in Tampere University

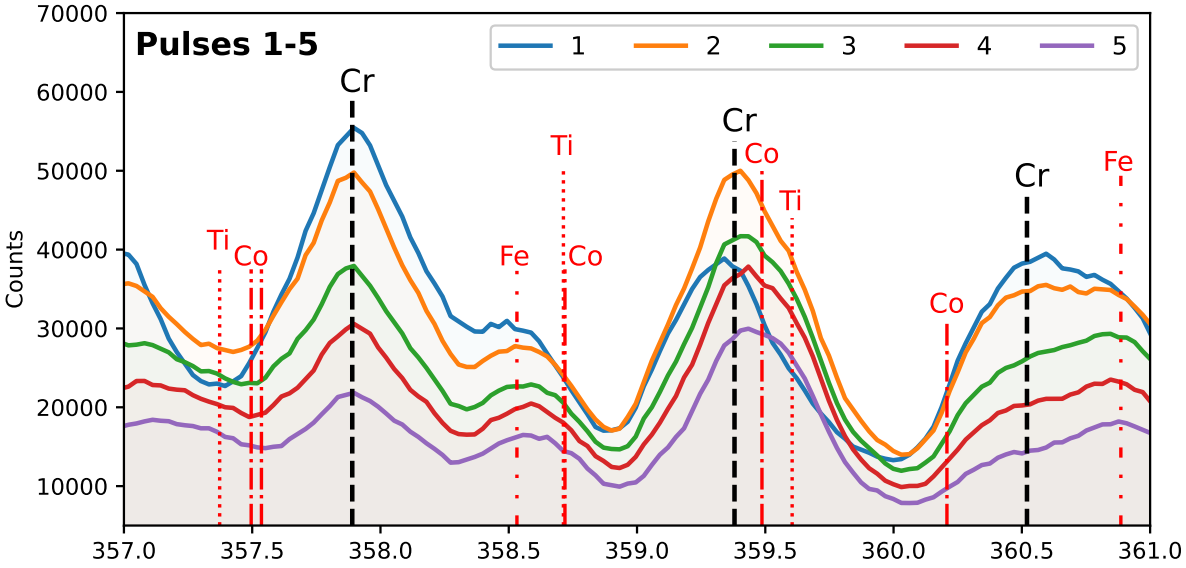

Figure 30. Individual LIBS spectra from sample 13 (0.45 % Cr) after 5 consecutive laser pulses. Measurement setup 2. The element emission lines marked with red are possible interference elements from the surface of the sample and from the coating.

In Tampere, the sample with the highest Cr content, sample 13 (0.45 %-Cr), was measured after 5 consecutive pulses. These spectra are shown in Figure 30. These spectra show how the signal measured from the plasma decreases in strength as each laser pulse ablates material from the sample and thus the hole gets deeper and limits the plasma formation and visibility to the collection lens system. The decrease is noticeable around at the 357.89 and 360.52 nm positions since the spectra have lower number of counts as the pulse number increases and. However, in every spectra the peaks at the 357.89 and 359.38 nm positions indicate the presence of Cr in the sample correctly but the peak at 360.52 nm is spread out and not as clear indication of Cr presence. These spectra do contain other elements in addition to chromium which disturbs them more than in the spectra measured in Jyväskylä for some reason.

Figure 31 presents sum spectra from eight samples with different Cr contents combining all the spectra after 50 laser pulses. The sample with the highest Cr content showed peaking at the Cr positions but not particularly clearly. In addition, the sample with the second-highest Cr content has a very low number of counts in the overall presented range. The 50 pulses used for the accumulation of these spectra was probably too high a number and also the laser energy was 27 mJ which most likely resulted in powerful ablation and

crater formation.

The spectra I obtained from Tampere LIBS measurements leave some room for improvement. I should have performed the more accurate pulse by pulse depth profiling to more than just the one sample with the highest Cr content.

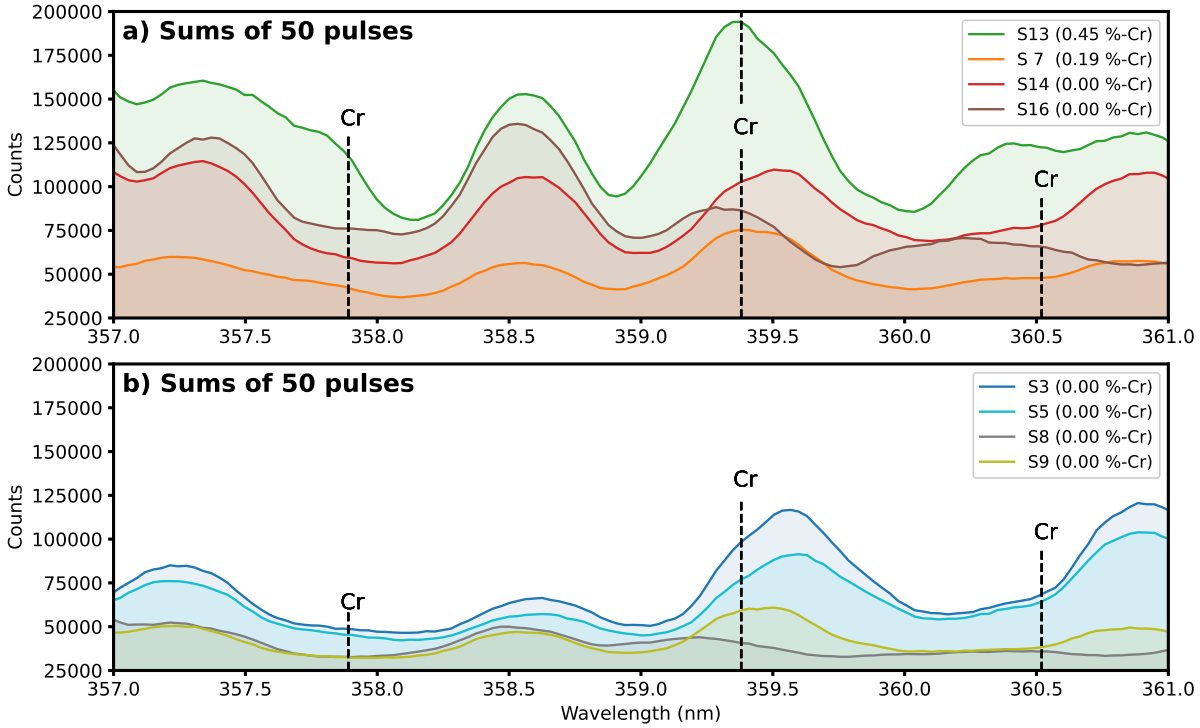

Figure 31. Sum spectra after 50 laser pulses from samples a) 13, 7, 14, and 16 and b) 3, 5, 8, and 9 with measurement setup 2 in Tampere.

6 Conclusions

The performance of XRF and LIBS were investigated in the detection of Cr impurity content of WC-Co samples. The difficulty in these samples were the varying thickness and composition of the coatings. Both methods proved to be useful in the detection of Cr content down to 0.45 mass% from the samples, provided that there are reference data from both kinds of samples; those that contain Cr and those that do not.

By comparing the measured spectra of the samples with multiple different setups, it seemed that XRF spectra for the samples can be separated by the presence of a peak at Cr Kα energy position. This applies for between samples that do not contain Cr at all and those that contain at least 0.19 % Cr. This position did not have interference from the measurement setup, other elements in the samples or from any artefacts from the detector. Cr Kβ peak proved to be more obscured and less reliable for different samples to be nothing but a factor that confirms whether the samples contained very high amounts of Cr (> 0.45 %). However, the type of detector did influence the resolution of Cr Kα peak a lot. CdTe detector provided a wider spectrum from a sample up to W kα energy but it was not as accurate at the Cr peak positions as SDD was. The superior resolution of SDD makes it a clear choice for the detection of the presence of Cr peaks in the spectra. However, the use of both types of detectors simultaneously can provide more detailed information about the overall element distribution of the samples. Also, a wavelength-dispersive XRF detector would be useful since it can be focused near the Cr energies.

As for the LIBS spectra from the samples, it seemed that they too can be used to distinguish between Cr containing samples and those that did not contain Cr. Special care needed to be taken when comparing peaks at Cr emission positions with Cr and non-Cr containing samples to prevent misinterpretation of the peaks. Since in LIBS spectrum all elements have very many emission peaks the possibility for mistakes in peak assigning is high. Nevertheless, wavelength positions of 357.89, 360.52, and 425.44 nm seemed to function well in distinguishing whether the sample in question contains 0.45 % Cr or more. The 425.44 nm position looked as the best of these since it had the least amount of disturbance in the background spectra.

An in-line purpose for an XRF measurement device sets some requirements for it.

The X-ray source needs to be powerful enough so it can produce enough primary X-rays for the Cr Kα peak to differentiate among other detected secondary X-rays in the short amount of time each sample piece is measured. The detector needs to have enough events-per-second capacity to detect large amount of X-rays in that short time the sample is at the measurement position. Also, in contrast to LIBS, the samples are not needed to be stopped in the in-line application, the beam size can be set to cover a wide area for the measurement of multiple samples at once, and there is no need to focus the beam to the surface plane of the samples.

Also LIBS has some specific requirements for it to be a viable in-line application. The laser pulse needs to be focused at the surface level of each individual sample that is measured with the setup. The laser energy needs to be high enough to ablate the possible coatings in a reasonable amount of pulses. However, it should not too powerful so that it makes too large a crater in the sample which makes the acquisition of proper spectra difficult.

Based on this work, I strongly belief XRF to be a more suitable candidate over LIBS for the purpose of detecting different Cr amounts in the kind of WC-Co hardmetal scrap pieces measured in this work. Since it was shown that XRF can detect and differentiate Cr amounts from the samples regardless of the possible coating of the provided samples, LIBS lost its main advantage: the ability to get rid of the coating and measure spectra from the bulk of the sample only. Given powerful enough X-ray source and an accurate detector with high resolution, XRF is very likely simpler and more reliable in an in-line environment than LIBS, since all samples can be measured without changing the system parameters when they are finetuned to fit into the system properly.

For this work only two sample pieces containing Cr were provided for measurements. Therefore, the results have little statistical value by themselves. However, by performing measurements to a wider selection of samples that contain differing amounts of chromium the statistical value of the results can be increased.

In the future more powerful X-ray source could be tested and verified that with such a source it is possible to satisfy the quick pace of measurement needed in an in-line environment. In addition a detector suitable for that source should be tested. Prototype station for in-line testing could be build with the equipment used in this work to test and optimize the mechanics and designs of the most efficient way of transporting, stopping and aligning the samples at the measurement spot. In addition, XRF measurement equipment suppliers should then be contacted and requested info about available setups matching

the needs of this specific application.

References

[1] E. Altuncu et al. “Cutting-tool recycling process with the zinc-melt method for obtaining thermal-spray feedstock powder (WC-Co)”. In: *Materiali in Tehnologije* 47 (Jan. 2013), pp. 115–118.

[2] B. Zeiler, A. Bartl, and W.-D. Schubert. “Recycling of tungsten: Current share, economic limitations, technologies and future potential”. In: *International Journal of Refractory Metals and Hard Materials* 98 (2021), p. 105546. ISSN: 0263-4368. DOI: https://doi.org/10.1016/j.ijrmhm.2021.105546.

[3] K. Brookes. “Hardmetals recycling and the environment”. In: *Metal Powder Report* 69.5 (2014), pp. 24–30. ISSN: 0026-0657. DOI: https://doi.org/10.1016/S0026-0657(14)70225-5.

[4] A. Shemi et al. “Recycling of tungsten carbide scrap metal: A review of recycling methods and future prospects”. In: *Minerals Engineering* 122 (2018), pp. 195–205. ISSN: 0892-6875. DOI: https://doi.org/10.1016/j.mineng.2018.03.036.

[5] M. Harada and K. Sakurai. “K-line X-ray fluorescence analysis of high-Z elements”. In: *Spectrochimica Acta Part B: Atomic Spectroscopy* 54.1 (1999), pp. 29–39. ISSN: 0584-8547. DOI: 10.1016/S0584-8547(98)00149-9.

[6] M. F. Gazulla et al. “Characterization of chromium-containing ceramic pigments by XRF and XRD”. In: *X-Ray Spectrometry* 33.6 (2004), pp. 431–438. DOI: https://doi.org/10.1002/xrs.745.

[7] I. Nakai et al. “Use of highly energetic (116keV) synchrotron radiation for X-ray fluorescence analysis of trace rare-earth and heavy elements”. In: *Journal of Synchrotron Radiation* 8.4 (2001), pp. 1078–1081. DOI: 10.1107/S0909049501006410.

[8] M. Yao, D. Wang, and M. Zhao. “Element Analysis Based on Energy-Dispersive X-Ray Fluorescence”. In: *Advances in Materials Science and Engineering* 2015 (2015). DOI: 10.1155/2015/290593.

[9] S. Wongsisa, P. Srichandr, and N. Poolthong. “Development of Manufacturing Technology for Direct Recycling Cemented Carbide (WC-Co) Tool Scraps”. In: *Materials transactions* 56.1 (2015), pp. 70–77. DOI: 10.2320/matertrans.M2014213.

[10] J. Pedarnig et al. “Review of Element Analysis of Industrial Materials by In-Line Laser—Induced Breakdown Spectroscopy (LIBS)”. In: *Applied Sciences* 11.19 (2021). ISSN: 2076-3417. DOI: 10.3390/app11199274.

[11] F. Anabitarte, A. Cobo, and J. M. Lopez-Higuera. “Laser-Induced Breakdown Spectroscopy: Fundamentals, Applications, and Challenges”. In: *ISRN Spectroscopy* 2012 (2012). DOI: 10.5402/2012/285240.

[12] R. Noll et al. “LIBS analyses for industrial applications – an overview of developments from 2014 to 2018”. In: *Journal of Analytical Atomic Spectrometry* 33 (6 2018), pp. 945–956. DOI: 10.1039/C8JA00076J.

[13] M. Holá et al. “Laser ablation for direct analysis of tungsten carbides”. In: *Hutní a průmyslová analytika 2007*. Václav Helán, 2007, pp. 45–50. ISBN: 978-80-86380-38-4.

[14] K. Novotný et al. “Analysis of powdered tungsten carbide hard-metal precursors and cemented compact tungsten carbides using laser-induced breakdown spectroscopy”. In: *Spectrochimica Acta Part B: Atomic Spectroscopy* 62.12 (2007), pp. 1567–1574. ISSN: 0584-8547. URL: https://www.sciencedirect.com/science/article/pii/S0584854707003382.

[15] W. C. Röntgen. “On a New Kind of Rays”. In: *Nature* 53.2 (1896), pp. 274–276. ISSN: 1369. DOI: 10.1038/053274b0. URL: https://doi.org/10.1038/053274b0.

[16] *The Nobel Prize in Physics 1901*. URL: https://www.nobelprize.org/prizes/physics/1901/summary/ (visited on 04/06/2022).

[17] R. Jenkins. *X-ray fluorescence spectrometry*. John Wiley & Sons, 2012.

[18] *Trajectory bending and energy spreading of charged ions in time-of-flight telescopes used for ion beam analysis*. URL: https://radiologykey.com/x-ray-production-2/# (visited on 01/13/2022).

[19] G. H. Zschornack. *Handbook of X-ray Data*. Springer Science & Business Media, 2007. ISBN: 978-3-540-28618-9.

[20] R. Jenkins et al. “Nomenclature, symbols, units and their usage in spectrochemical analysis-VIII. Nomenclature system for X-ray spectroscopy (Recommendations 1991)”. In: *Pure and applied chemistry* 63.5 (1991), pp. 735–746.

[21] E. Margui and R. Van Grieken. *X-ray fluorescence spectrometry and related techniques: an introduction*. Momentum press, 2013.

[22] G. F. Knoll. *Radiation detection and measurement*. John Wiley & Sons, 2010. ISBN: 9780470131480.

[23] G. V. Pavlinsky. *Fundamentals of X-ray Physics*. Cambridge International Science Publishing Ltd, 2008.

[24] D. K. Schroder. *Semiconductor material and device characterization*. 3rd ed. John Wiley & Sons, 2006. ISBN: 978-0-471-74908-0.

[25] P. Palmer. *Introduction to energy-dispersive X-ray fluorescence (XRF) – An analytical chemistry perspective*. URL: https://www.asdlib.org/onlineArticles/ecourseware/Palmer/ASDL%5C%20Intro%5C%20to%5C%20XRF.pdf (visited on 02/02/2022).

[26] *ThermoScientific XL5 Plus XRF Analyzer: Product Specification*. URL: https://www.thermofisher.com/document-connect/document-connect.html?url=https%5C%3A%5C%2F%5C%2Fassets.thermofisher.com%5C%2FTFS-Assets%5C%2FCAD%5C%2FDatasheets%5C%2Fniton-xl5-plus-spec-sheet.pdf (visited on 04/25/2022).

[27] J. C. Lindon, G. E. Tranter, and D. Koppenaal. *Encyclopedia of spectroscopy and spectrometry*. Academic Press, 2016. ISBN: 9780128032251.

[28] J. Fink et al. "Characterization of charge collection in CdTe and CZT using the transient current technique". In: *Nuclear Instruments and Methods in Physics Research Section A: Accelerators, Spectrometers, Detectors and Associated Equipment* 560.2 (May 2006), pp. 435–443. ISSN: 0168-9002. DOI: 10.1016/j.nima.2006.01.072.

[29] Y. Liao. *Practical electron microscopy and database*. 2006, p. 4655. URL: https://www.globalsino.com/EM/page4655.html/ (visited on 03/12/2022).

[30] R. Redus et al. "Design and performance of the X-123 compact X-ray and gamma-ray spectroscopy system". In: *IEEE Nuclear Science Symposium Conference Record*. Vol. 6. IEEE. 2006, pp. 3794–3797.

[31] R. Redus et al. "Characterization of CdTe detectors for quantitative X-ray spectroscopy". In: *IEEE Transactions on Nuclear Science* 56.4 (2009), pp. 2524–2532.

[32] R. Redus et al. “CdTe Detectors for Quantitative X-Ray Fluorescence”. In: *2007 Denver X-ray Conference*. Amptek Inc. 2007. URL: https://www.amptek.com/products/x-ray-detectors/cdte-x-ray-and-gamma-ray-detectors/cdte-x-ray-and-gamma-ray-detector (visited on 03/21/2022).

[33] J. Nishizawa et al. “Effects of Heating on Electrical and Spectral Properties of In/CdTe/Au X- and -ray Detectors with a Schottky Barrier or Laser-induced p–n Junction”. In: *Sensors and Materials* 32.11 (2020), pp. 3801–3812. DOI: 10.18494/SAM.2020.3054.

[34] P. Lechner et al. “Hard x-ray and gamma-ray imaging and spectroscopy using scintillators coupled to silicon drift detectors”. In: *High Energy, Optical, and Infrared Detectors for Astronomy III*. Ed. by D. A. Dorn and A. D. Holland. Vol. 7021. International Society for Optics and Photonics. SPIE, 2008, pp. 348–357. DOI: 10.1117/12.788803.

[35] *Silicon Drift Detectors Explained (OINA/SDDExplained/0212)*. 2012. URL: https://nano.oxinst.com/products/sem-and-fib (visited on 01/13/2022).

[36] G. Lutz et al. *Semiconductor radiation detectors*. Springer, 2007. ISBN: 978-3-540-71678-5.

[37] Y. Liao. “Practical electron microscopy and database”. In: *An Online Book* (2006). URL: https://www.globalsino.com/EM/ (visited on 01/13/2022).

[38] A. K. Maini. *Lasers and Optoelectronics : Fundamentals, Devices and Applications*. New York: John Wiley & Sons, Incorporated, 2013. DOI: 10.1002/9781118688977.

[39] J. Singh and S. Thakur. *Laser-Induced Breakdown Spectroscopy*. Elsevier, 2007. ISBN: 9780444517340. DOI: 10.1016/B978-0-444-51734-0.X5001-7.

[40] R. Noll. *Laser-Induced Breakdown Spectroscopy*. Springer-Verlag, 2012. ISBN: 978-3-642-20667-2. DOI: 10.1007/978-3-642-20668-9.

[41] A. Miziolek, V. Palleschi, and I. Schechter. *Laser Induced Breakdown Spectroscopy*. Cambridge University Press, 2006. DOI: 10.1017/CBO9780511541261.

[42] D. A. Cremers and L. J. Radziemski. *Handbook of Laser-Induced Breakdown Spectroscopy*. 2nd ed. John Wiley & Sons, Ltd, 2013. ISBN: 9781118567371. DOI: 10.1002/9781118567371.

[43] K. Frenk. *Basics of Laser Physics. For Students of Science and Engineering*. 2nd ed. Springer Cham, 2017. DOI: 10.1007/978-3-319-50651-7.

[44] H. Becker-Ross and S. Florek. “Echelle spectrometers and charge-coupled devices”. In: *Spectrochimica Acta Part B: Atomic Spectroscopy* 52.9 (1997). Second European Furnace Symposium, pp. 1367–1375. ISSN: 0584-8547. DOI: https://doi.org/10.1016/S0584-8547(97)00024-4.

[45] J. B. Kortright and A. C. Thompson. *X-Ray Data Booklet: Section 1.2: X-ray Emission Energies: Table 1-2*. Center for X-ray Optics and Advanced Light Source, 2009. URL: https://xdb.lbl.gov/Section1/Table_1-2.pdf (visited on 10/11/2021).

[46] *NIST Material Details SRM 1157 Tool Steel (AISI M2)*. URL: https://www-s.nist.gov/srmors/view_detail.cfm?srm=1157 (visited on 10/11/2021).

[47] A. Kramida et al. *NIST Atomic Spectra Database (version 5.8)*. DOI: 10.18434/T4W30F. URL: https://physics.nist.gov/asd (visited on 10/11/2021).

[48] V. Solé et al. “A multiplatform code for the analysis of energy-dispersive X-ray fluorescence spectra”. In: *Spectrochimica Acta Part B: Atomic Spectroscopy* 62.1 (2007), pp. 63–68. ISSN: 0584-8547. DOI: https://doi.org/10.1016/j.sab.2006.12.002.

[49] J. Kruth et al. “Computed tomography for dimensional metrology”. In: *CIRP Annals* 60.2 (2011), pp. 821–842. ISSN: 0007-8506. DOI: https://doi.org/10.1016/j.cirp.2011.05.006. URL: https://www.sciencedirect.com/science/article/pii/S0007850611002083.

[50] J. Als-Nielsen and D. McMorrow. *Elements of modern X-ray physics*. John Wiley & Sons, 2011.

[51] W. R. Leo. *Techniques for nuclear and particle physics experiments: a how-to approach*. Springer Science & Business Media, 2012.

[52] R. Van Grieken and A. Markowicz. *Handbook of X-ray Spectrometry*. CRC press, 2001.

A XRF and LIBS spectra of WC-Co samples containing 0 % Cr

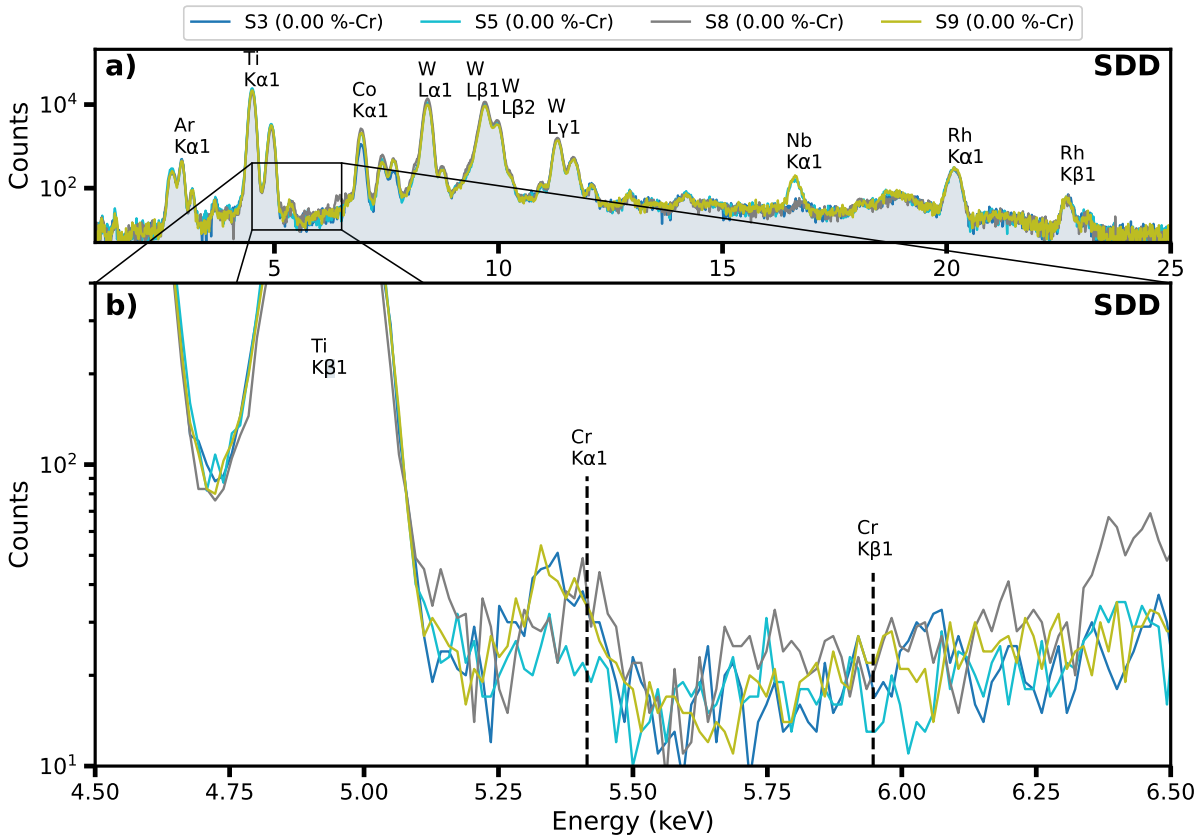

Figure A1. The spectra of samples 3, 5, 8, and 9 measured with XRF measurement setup 2. All samples have a Cr content of 0.00 %. Figure a) shows the full spectra and Figure b) the spectra near Cr Kα energy. Peaking at that energy is not as strong as in the samples that had 0.19 and o.45 % Cr in them. Still, it can not be concluded that the 0.00 % samples here did not contain Cr at all, they may contain small amounts of it.

To provide more data for the backing up of the results and conclusions of this work, in this appendix spectra from four samples (3, 5, 8, and 9) that did not contain any Cr, according to the reference data by Tikomet, are presented. Figure A1 shows the XRF spectra for these four samples. There is slight peaking at Cr Kα position but not as

strong as in the samples that contained Cr according to the reference data. Therefore, these samples may contain small amounts of Cr which would be responsible for the small peaking. At Cr Kβ position the spectra have practically nothing but the bremsstrahlung visible.

As for LIBS, similar sets of spectra after three consecutive pulses are presented in Figures A2 and A3 as were for samples that contained Cr. In Figure A2 there are no peaks at Cr emission line positions. In Figure A3 there are peaking near the 427.49 and 428.99 nm positions even though the samples do no contain Cr according to the reference data. This is an important observation because it further strengthens the decision of not focusing on these positions when determining the presence of Cr in the sample. Also, the 425.44 nm position in Figure A3 is shown to be a good position as a Cr indicator from these kind of samples.

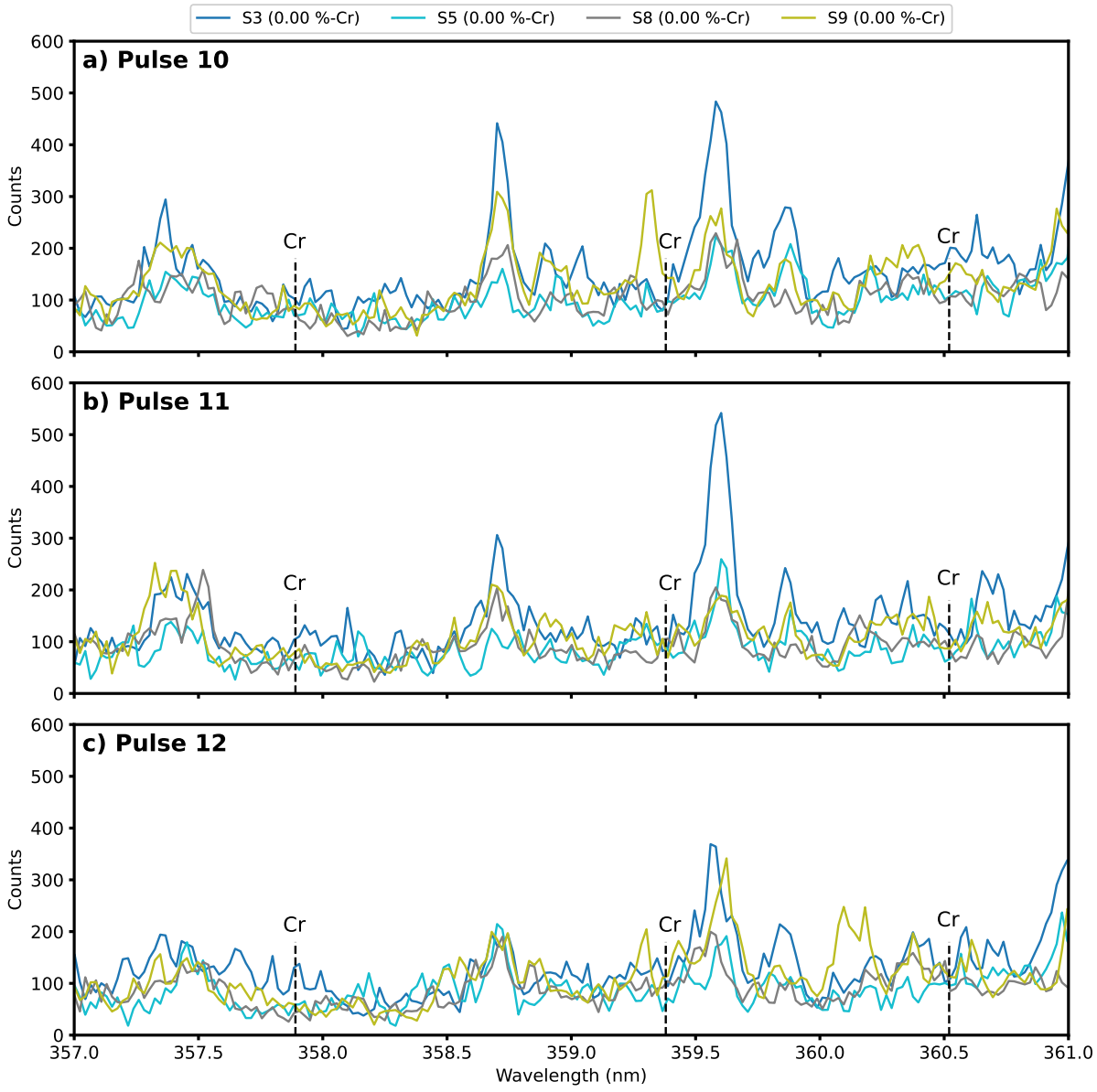

Figure A2. LIBS spectra of samples 3, 5, 8, and 9 after three separate pulses, those pulses being 10^{th}, 11^{th}, and 12^{th}. No clear peaking is detectable at the energies of Cr emission lines.

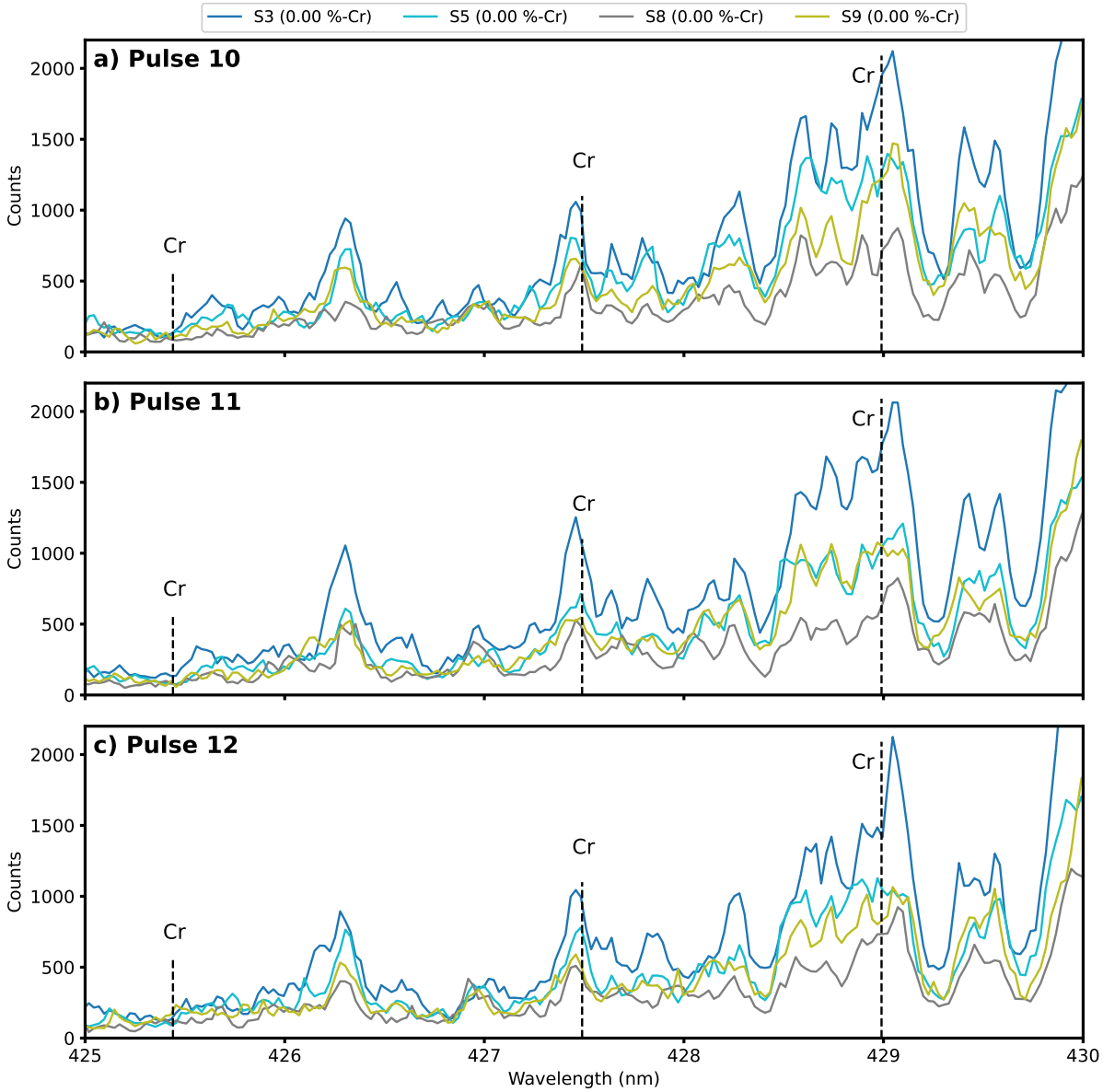

Figure A3. LIBS spectra of samples 3, 5, 8, and 9 after pulses 10, 11, and 12. No clear peaking is detectable at the 425.44 nm position, however, the 427.49 and 428.99 nm positions show a lot of peaking probably caused by other elements of the samples.